energies

Article

Evaluation of the Effects of Yielding Rockbolts on Controlling Self-Initiated Strainbursts: A Numerical Study

Jun Wang [1], Derek B. Apel [1,*], Huawei Xu [1], Chong Wei [1] and Krzysztof Skrzypkowski [2,*]

1 School of Mining and Petroleum Engineering, University of Alberta, Edmonton, AB T6G 2R3, Canada; jun8@ualberta.ca (J.W.); hx1@ualberta.ca (H.X.); cwei4@ualberta.ca (C.W.)
2 Faculty of Civil Engineering and Resource Management, AGH University of Science and Technology, 30-059 Kraków, Poland
* Correspondence: dapel@ualberta.ca (D.B.A.); skrzypko@agh.edu.pl (K.S.)

Abstract: In this paper, a 2D distinct element method (DEM) model of a deep tunnel in an underground coal mine is built to thoroughly evaluate the effects of yielding (D-bolt and Roofex) and the traditional rockbolt (fully resin-grouted rebar) on controlling self-initiated strainbursts. The occurrence of self-initiated strainbursts is judged based on the stiffness difference between the loading system and rock masses for the first time. The results suggest that the total deformations of the tunnel supported with Roofex and resin-grouted rebar are 1.53 and 2.09 times that of D-bolts (1411 mm). The average velocities of detached rock blocks in the tunnel supported with Roofex and resin-grouted rebar are 3.22 and 3.97 m/s, respectively, which are much higher than that of D-bolts (0.34 m/s). 13 resin-grouted rebar bolts are broken during the strainburst, while D-bolts and Roofex survive. Compared with Roofex (295.16 kJ) and resin-grouted rebar (125.19 kJ), the D-bolt can reduce the most kinetic energy (469.30 kJ). D-bolt and resin-grouted rebar can maintain high axial force levels (214.87 and 151.05 kN) during strainbursts. Both Roofex and resin-grouted rebar fail to control strainbursts. The bolt number significantly influences the control effects of yielding rockbolts on strainbursts. 9 and 12 D-bolts cannot control the strainburst, while 15 and 18 D-bolts can make the tunnel stable. In addition, the detachment and ejection of rocks between rockbolts can be well restrained using surface retain elements, e.g., steel arch. This study highlights the usage of numerical modeling methods in assessing the performance of yielding rockbolts, which can be served as a promising tool to improve and optimize the design of rock supporting in burst-prone grounds.

Keywords: strainburst; local mine stiffness; yielding rockbolt; numerical modeling; distinct element method; underground mining

check for updates

Citation: Wang, J.; Apel, D.B.; Xu, H.; Wei, C.; Skrzypkowski, K. Evaluation of the Effects of Yielding Rockbolts on Controlling Self-Initiated Strainbursts: A Numerical Study. *Energies* **2022**, *15*, 2574. https://doi.org/10.3390/en15072574

Academic Editor: Maxim Tyulenev

Received: 24 February 2022
Accepted: 28 March 2022
Published: 1 April 2022

1. Introduction

Strainburst is an unstable rock failure phenomenon at excavation boundaries of deep tunnels in mining and civil engineering projects. It is characterized by the sudden and violent ejection of rock materials. Strainburst is the most common type of rockbursts in all underground excavations [1]. It can damage equipment and facilities, which will further delay production and cause tremendous economic loss [2]. Worse still, strainburst can also result in many injuries and fatalities [3]. Hence, much work needs to be conducted to control and mitigate strainburst damage.

Generally, strainburst can be classified into two types: self-initiated and remotely triggered [4]. The self-initiated strainburst occurs due to the concentration of excavation-induced tangential stress and the existence of a relatively "soft" loading environment in the rock mass surrounding the fracturing rock [5]. There is not a remote seismic event involved in self-initiated strainbursts. The remotely triggered strainburst is caused by the combination of a remote seismic event triggered by large-scale mining activities and high static stress [6,7]. Self-initiated strainburst is a more frequently encountered type of strainbursts, because it happens in both mining and civil engineering projects while remotely triggered strainburst usually occurs only in mining environments [7]. This study specifically focuses on the investigation of the control of self-initiated strainbursts.

To date, many measures and strategies have been proposed to control and mitigate strainburst damage. For instance, distress drilling and blasting are two standard measures to reduce strainburst risks by transferring concentrated stresses to rock masses in-depth. Another common tactic is using yielding rockbolts. This type of rockbolts allows yielding to absorb more kinetic energy and have higher displacement capacities than conventional rockbolts (e.g., expansion-shell bolt and rebar bolt). Hence, yielding rockbolts can resist the dynamic loads and accommodate large deformation caused by rock fracturing, dilation, and ejection during strainbursts [7]. In the last several decades, many different types of yielding rockbolts have been developed to control rockbursts, e.g., Cone bolt [8], Roofex [9,10], Garford bolt [11], D-Bolt [12,13], Yield-Lok [14], and He-bolt [15].

A critical task is to evaluate the effects (e.g., control of rock damage and the capacity of energy-absorption) of yielding rockbolts on controlling strainbursts before being widely used. The methodologies to study rockbolt performance mainly include field tests [16–18], laboratory test, and numerical modeling. The field test method can obtain real-time data and assess the in situ performance of rockbolts, but they are usually time-consuming, expensive, and dangerous, especially in burst-prone grounds. Compared with field tests, the experimental methods have the advantages of repeatability, safety, and flexibility [19]. At present, the evaluation of the rockbolt performance in strainburst conditions is conducted mainly using the drop test [10–12,20–22]. The research has achieved many positive outcomes, providing excellent references for understanding the behavior of different types of yielding rockbolts under dynamic impacts. However, the drop test is straightforward and is only a crude simulation of rockburst loading. The complex interaction between seismic waves, rockbolts, and reinforced rock masses is not considered. For instance, Bosman et al. [23] stated that the dynamic capacity of a rockbolt is not a constant value, and the loading mode of a rockbolt will affect its dynamic capacity. Therefore, the impact loading from conventional drop tests might not represent rockburst loading. Wu et al. [18] also pointed out that the impact load in drop tests cannot represent the impact of ground pressure load, and the existing test system generally cannot reproduce the complex ground support/rock mass interaction that exists in an underground environment. Besides, original rock stress is not considered in tests.

With the rapid development of information technology (IT) and computer equipment, various numerical methods and codes have been developed and employed to simulate complex physical phenomena in rock mechanics and rock engineering [24–27]. The numerical simulation methods have been acknowledged as effective research and engineering design tools as it can represent the realistic mechanical behavior of rock masses and support elements with rational input data (e.g., excavation size and shape, material properties, and boundary conditions) and calibration procedures [28]. Nie et al. [29] developed rockbolt models using DDA to investigate the failure mechanism of an expansion-shell bolt, fully grouted rebar, split set, and D-bolt in simulated pull-out and drop tests. Marambio et al. [30] modeled a laboratory-scale test via FLAC3D to study the performance of threadbar in dynamic loading. The simulation results matched well with laboratory observations. Yokota et al. [31] assessed a self-developed deformation-controlled rockbolt (DC-bolt)'s behavior in tunnel supporting via DDA simulation. Zhang and Nordlund [19] employed the UDEC program to investigate the differences of dynamic performances of a fully grouted rebar between the simulated drop tests and seismic loading in the configuration where two slightly separated rock bars were used. Zhao et al. [32] studied the influence of structure element position on the anchoring effect of energy-absorption bolts via simulating pull-out tests in FLAC3D.

In summary, most current work focuses on evaluating the performance of traditional rockbolts under dynamic loading, while some researchers try to simulate the dynamic behavior of yielding rockbolts by reproducing drop tests. Few numerical studies have been reported to assess the performance of yielding rockbolts during self-initiated strainbursts with actual seismic loading. As mentioned above, the impact loading in drop tests might not represent rockburst loading, and the rock stress is also absent. Hence, the complex interaction between seismic waves, rockbolts, and reinforced rock masses during self-initiated strainbursts with explicit rock detachment and ejection (requiring the distinct element method (DEM) or DEM-related hybrid methods) needs to be further numerically investigated.

This study aims to evaluate the effects of yielding rockbolts on controlling self-initiated strainbursts using DEM modeling. The rationality and capability of DEM software UDEC in modeling self-initiated strainbursts are first validated through comparison with laboratory tests. Then, two types of yielding rockbolts (Roofex and D-bolt) and the traditional rockbolt (fully resin-grouted rebar, for comparison) are modeled via the "rockbolt" element in UDEC after an exact calibration procedure. Instead of conventional drop tests, a 2D model of a deep tunnel in an underground coal mine is built to fully evaluate the performance (e.g., the dynamic capacity of energy absorption and control of rock damage) of yielding and traditional rockbolts during simulated strainbursts. The occurrence of self-initiated strainbursts is judged based on the stiffness difference between the loading system and rock masses for the first time.

2. Validation of UDEC in Modeling Self-Initiated Strainbursts

2.1. Brief Introduction of the True Triaxial Experiments of Self-Initiated Strainbursts

Considering that the self-initiated strainburst is a structural failure of rock masses near the excavation boundary, Su et al. [33,34] conducted a series of true triaxial tests of rock samples by reproducing strainbursts in a self-developed true triaxial testing facility (see Figure 1a,b). In tests, rock samples with the dimension of 100 mm (length) × 100 mm (width) × 200 mm (height) were used to simulate the burst volume of a representative rock element (RRE) (Figure 1c,d). The cracking and ejecting processes of rock samples during strainbursts were monitored by an acoustic emission (AE) system and two high-speed cameras. The tangential stress concentration and radial stress distribution of near-boundary rock masses were simulated by a loading path that keeps one face free and loads on the other faces (Figure 1c). The detailed test procedures are as follows: (1) maintain one face of the rock sample free (y-direction) and apply loads to the other five faces simultaneously to a pre-defined initial stress state; (2) maintain stresses in x and y directions, and increase the stress in z-direction until the strainburst occurs.

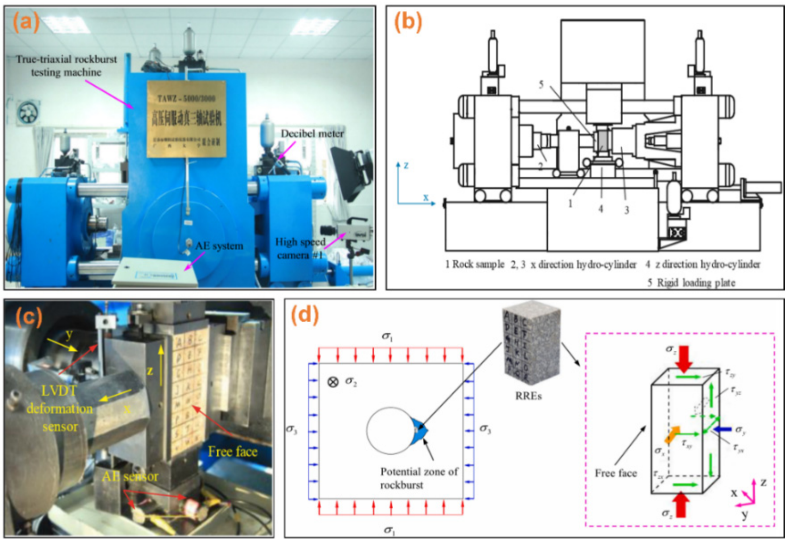

Figure 1. A true triaxial strainburst testing facility: (**a**,**b**) are the loading configuration; (**c**) is the stressed rock sample; (**d**) shows the boundary conditions and stress state of the rock sample ((**a**) is from Su et al. [34]; (**b**–**d**) are from Hu et al. [35]).

2.2. Validation of UDEC Simulation

In order to validate the reliability and accuracy of the 2D distinct element code UDEC in modeling self-initiated strainbursts, numerical simulation results were compared with the laboratory test results from Hu et al. [35]. The model configuration, including the model dimension, block shape and size, material properties, constitutive models, and loading mode, are the same as those used by Hu et al. [36,37]. The only difference is that the 3D distinct element code 3DEC rather than UDEC was employed in their studies.

A Trigon approach developed by Gao et al. [38] was used to generate blocks in the model (Figure 2a), as this approach is capable of reproducing the realistic fracturing processes (e.g., crack initiation, propagation, and coalescence) of rocks without adopting complicated constitutive models [39–41]. In the Trigon approach, a rock or rock mass is represented as an assembly of triangular blocks bonded together by contacts [38]. The fracturing process can be exhibited either by the sliding or opening of contacts. In the simulation, the blocks have an average edge length of 6 mm, which was sufficiently fine to simulate the failure behavior of rocks [36,37]. The material properties of blocks and contacts are listed in Table 1. In order to trigger a strainburst (unstable failure), the top platen has a lower stiffness (4 GN/m) than the post-peak characteristic stiffness of the rock sample (4.51 GN/m), which represents a soft loading system. Accordingly, Young's modulus and length of the top platen are 40 GPa and 100 mm, respectively. The stiffness of lateral and bottom platens are 1372 GN/m and 686 GN/m, respectively, representing much stiff loading systems, and thus the loading system stiffness (LSS) effect can be ignored [42].

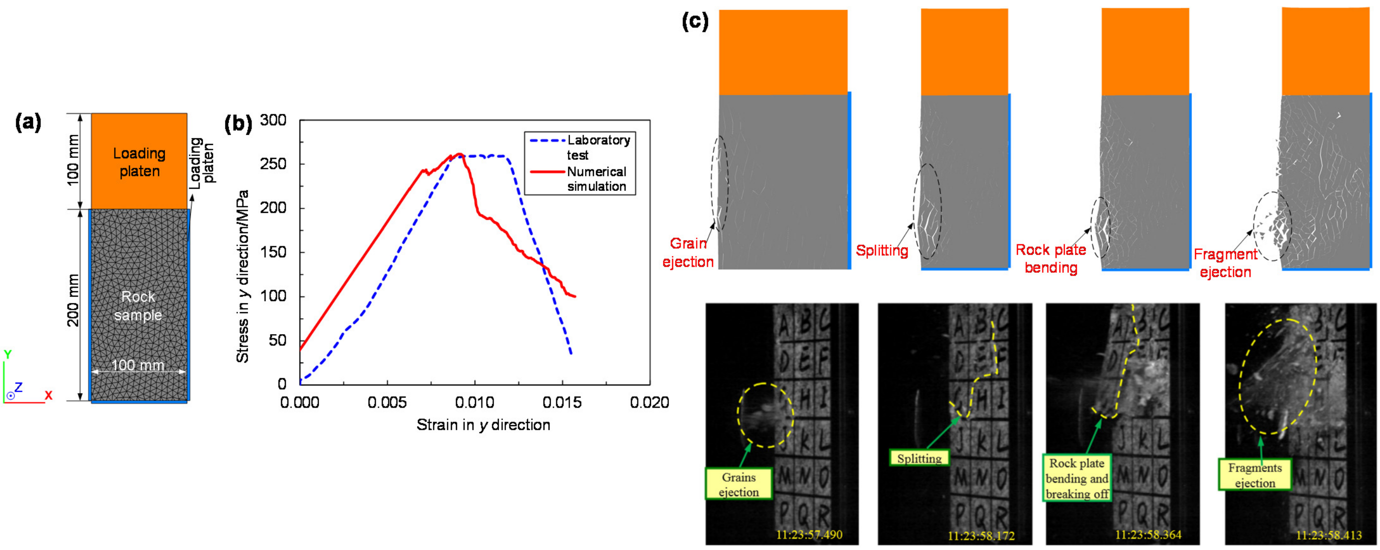

Figure 2. A numerical model for simulating self-initiated strainbursts and the comparison between the simulation and experimental results: (**a**) numerical model; (**b**) stress-strain curves obtained by the simulation and laboratory test [35]; (**c**) comparison between simulated failure stages and modes and experimental observations [35].

Table 1. Material properties used in the model [36,37].

Items	**Block Properties**			**Contact Properties**							
	ρ (kg/m^3)	**K (GPa)**	**G (GPa)**	**k_n (GPa/m)**	**k_s (GPa/m)**	**c^j (MPa)**	**$c_r{}^j$ (MPa)**	**φ^j (°)**	**$\varphi_r{}^j$ (°)**	**$\sigma_t{}^j$ (MPa)**	**$\sigma_{tr}{}^j$ (MPa)**
Granodiorite	2650	21.22	12.12	210,000	83,370	52	0	61.5	22	13	0
Top platen	7700	33.33	15.38					-			
Other platens	7700	171.67	79.23					-			
Interface between platens and rock sample		-		210,000	83,370	0	0	14.57	0	0	0

Note: ρ, K, and G are the bulk density, bulk modulus, and shear modulus of blocks. k_n and k_s are the normal and shear stiffness of contacts. c^j, φ^j, and $\sigma_t{}^j$ are the cohesion force, internal friction angle, and tensile strength of contacts. $c_r{}^j$, $\varphi_r{}^j$, and $\sigma_{tr}{}^j$ are the residual values of cohesion forces, internal friction angle, and tensile strength of contacts.

The simulation was implemented as following procedures: (1) A pre-defined initial stress state (σ_x = 5 MPa, σ_y = 45 MPa, and σ_z = 30 MPa) was applied to the model, and the "geostatic equilibrium" was achieved after sufficient calculation steps [36,37]. The model boundaries were initially fixed to simulate the in situ state. (2) One lateral platen and its boundary conditions in x-direction were removed, while other boundary conditions remained unchanged. A constant velocity of 0.1 m/s was applied to the surface of the top platen until the peak strength (y-direction) was reached. (3) The dynamic mode in UDEC was activated. The local damping ratio was set at 0.05 after a trial-and-error process. The boundary conditions (e.g., fixed boundary) used in the static stage can cause the reflection of outward propagating waves back into the model and do not allow the necessary energy radiation. Thus, the viscous boundary developed by Lysmer and Kuhlemeyer [43] was used in the dynamic calculation.

The comparison between the simulated results and laboratory test results is shown in Figure 2b,c. It can be seen that the stress-strain curve, failure stages, and failure modes including grain ejection, splitting and bending of rock plates, and fragment ejection during the strainburst test, can be realistically captured by numerical modeling. Hence, the capability and accuracy of UDEC in modeling the self-initiated strainburst are validated. In Hu et al. [36,37], they needed to compare simulation results with laboratory test results of cuboid rock samples and investigate the influence of intermediate stress on indoor strainburst failure. Thus, the 3D program 3DEC was used in their research. As mentioned above, strainbursts usually occur at the excavation boundary of a tunnel in a high geo-stress environment. Therefore, if there are no nearby excavations, the plane strain assumption of a 2D model would be rational. The accuracy of UDEC in modeling the self-initiated strainburst has also been verified with experimental results in this study. Besides, the employment of UDEC can significantly reduce the calculation cost compared with 3DEC. Figure 3 shows an example that the run time of 3DEC is around 90 times that of UDEC when dealing with the same problem, indicating that UDEC is more productive than 3DEC. Therefore, UDEC is adopted considering both reliability and efficiency.

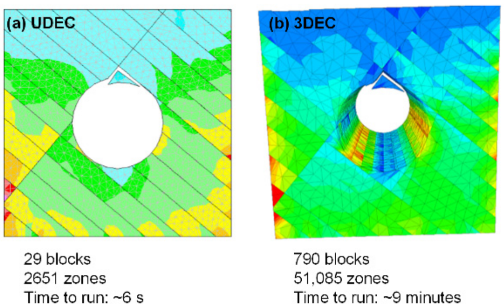

Figure 3. An example about the comparison of the run time between UDEC and 3DEC [44].

3. Numerical Modeling

3.1. Model Setup

3.1.1. Model Dimensions and Boundary Conditions

The simulation of the self-initiated strainburst at a laboratory scale is helpful to understand its detailed damage mechanisms (e.g., fracturing process and failure mode). However, the complex interaction between rockbolts and reinforced rock masses during strainbursts is hard to capture in this model setup due to the size limit, which prevents the model from being a potential design tool of rockbolting in burst-prone grounds. Therefore, to analyze the performance of rockbolts more realistically and accurately, the self-initiated strainburst occurring in a deep tunnel in an underground coal mine was modeled in this research rather than simulating it at a laboratory scale as previous studies. A widely used 2D DEM software UDEC was used to construct the numerical model. The model size is 30 m $\times$ 25 m. The shape of the tunnel cross-section is semicircular, with width and height of 6 m and 4 m, respectively. Figure 4 shows the geometry of the numerical model, which is based on the lithology and designed size of a deep coal mine drift.

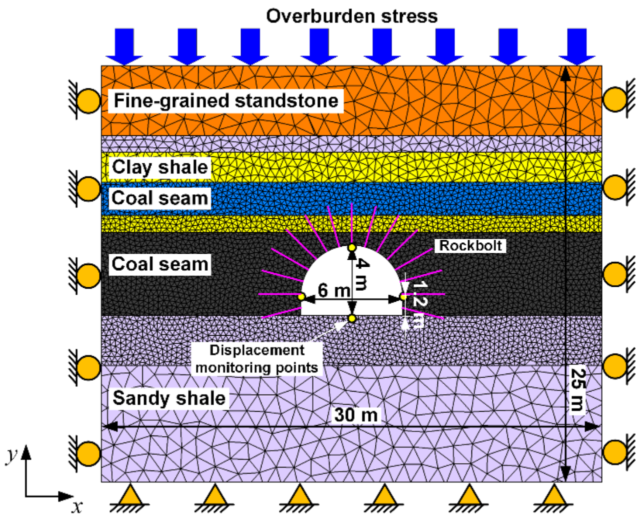

Figure 4. 2D numerical model of a deep tunnel in an underground coal mine.

The rock masses are divided into triangular blocks using the Trigon approach [38]. In the model, the average edge length of the blocks in two coal seams and nearby clay shale between them was set to 0.3 m. The block size with a range of 0.2–0.5 m was sufficiently acceptable to simulate the failure behavior of surrounding rock masses for a 2D model [38–40]. The average edge length of the blocks in the upper clay shale, sandy shale, and fine-grained sandstone was set to 0.5 m, 0.5 m, and 1 m, respectively. The average edge length of the blocks on the floor was set to 0.3 m and 1 m. A graded increasing edge length of blocks can avoid the resulting loss of simulation accuracy and enhance the calculation's reliability.

The upper boundary of the model was free and vertical stress of 24.3 MPa (assume the unit weight of overburden is 0.027 MN/m^3 and the buried depth is 900 m) was applied to the upper boundary to simulate the overburden weight. The roller constraints were applied on lateral boundaries, and the bottom boundary was fixed during the static stage (Figure 4). The ratio of horizontal to vertical stress (K) was assumed to be one since the hydrostatic stress state is a general in situ stress state in many deep excavations [45].

3.1.2. Modeling Large-Scale Strainbursts Based on the Stiffness Theory

The loading system stiffness (also called local mine stiffness at the engineering scale) and the post-failure stiffness of rock materials can distinguish stable or unstable failure (rockburst) effectively based on the stiffness theory [46]. If the loading system stiffness is smaller than the post-failure stiffness, the failure will be unstable and violent because the excess energy will transfer to the kinetic energy of ejected rocks. When the research object is a rock sample (e.g., [36,37]), it is simple to obtain the loading system stiffness K_L by the following equation:

$$K_L = \frac{AE}{L} \tag{1}$$

where A is the cross-section area of the loading platen; E is Young's modulus of the loading platen; L is the loading platen length.

However, unlike the unstable failure of rock samples, it is hard to identify the loading system when the focus is a strainburst that usually occurs in a tunnel or roadway. Thus, the determination of local mine stiffness becomes a more difficult task. Jaiswal and Shrivastva [47] proposed a method for calculating the local mine stiffness of a rock pillar by numerical modeling. The local mine stiffness is defined as a ratio of the load F_1 applied on the rock pillar over the distance difference ($d_1 - d_2$) with and without the modeling of the rock pillar (Figure 5a). This study adopted this logic to calculate the local mine stiffness for a tunnel (see Figure 5b). In Stage 1, the internal pressure P_1 at the planned excavation boundary equals the in situ stress P_i. In Stage 2, P_1 is reduced to zero (P_2) after excavation. Similar to the calculation method of a rock pillar, the local mine stiffness for a tunnel can be determined as follows:

$$K_L = \frac{P_1}{(d_1 - d_2)} = \frac{P_i}{U} \quad (2)$$

where d_1 and d_2 are the tunnel diameter before and after excavation; U is the convergence of tunnel walls after excavation. This method is the first attempt to calculate the local mine stiffness for a tunnel to the authors' knowledge. The excavation of the deep coal mine drift was simulated to obtain the local mine stiffness using the proposed method in this research. The obtained local mine stiffness is 174 MPa, where the tunnel convergence has been normalized by the tunnel diameter for convenient comparison with the post-peak characteristic stiffness of rock masses.

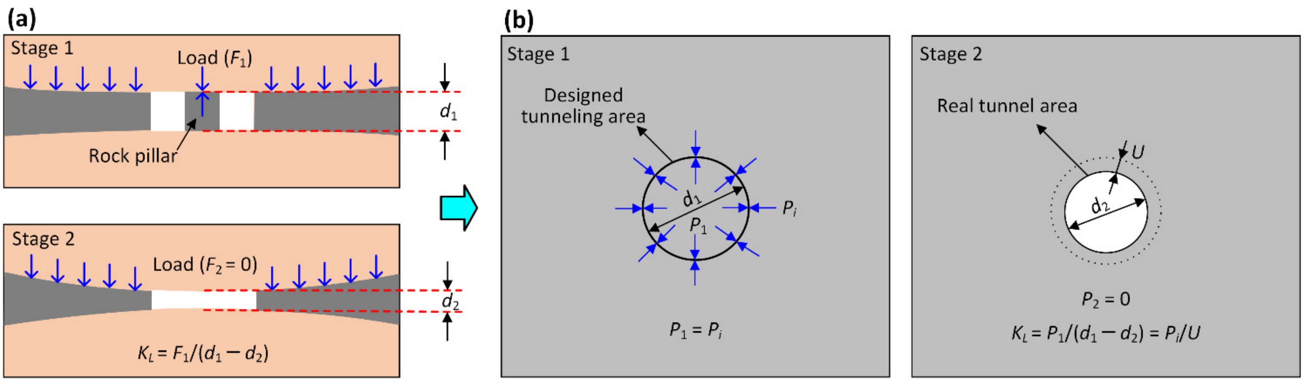

Figure 5. Determination of local mine stiffness by numerical modeling. (**a**) Local mine stiffness calculation for a rock pillar (after Jaiswal and Shrivastva [47]). (**b**) Proposed calculation method of local mine stiffness for a tunnel.

Since the main surrounding rock masses are coal seam and its strength is much lower than clay shale and sandy shale, only the post-peak characteristic stiffness of coal masses is determined using simulated uniaxial compression strength (UCS) tests. Considering that the rock mass property (e.g., strength and stiffness) is scale-dependent [48], the dimension of the rock mass model was determined based on the representative elementary volume (REV) concept [49]. The REV refers to the minimum scale of rock masses beyond which the material property becomes independent of the sample size (see Figure 6a). According to Bieniawski [50] (see Figure 6b), the UCS of coal masses declines gradually with increased sample side length. When the sample side length is less than 1.5 m, the UCS decreases remarkably with the growth of the specimen size. However, the UCS approaches a plateau when the sample side length exceeds 1.5 m, indicating that the scale dependency could be negligible. Thus, the REV size of the coal mass should be at least 1.5 m. In this study, the UCS model size is 4 m × 8 m, sufficient to eliminate the scale dependency. This model size is identical to Yang et al. [40].

Figure 7a shows the numerical model of UCS tests. In order to obtain the post-peak characteristic stiffness of the coal mass sample, the bulk and shear moduli of loading platens were set at an extremely high value (1000 GPa) to simulate an ideal rigid loading condition. As shown in Figure 7b, the obtained post-peak characteristic stiffness is 255 MPa, greater than the local mine stiffness (174 MPa). Hence, the self-initiated strainburst can happen. The material properties associated with coal masses are listed in Tables 2 and 3.

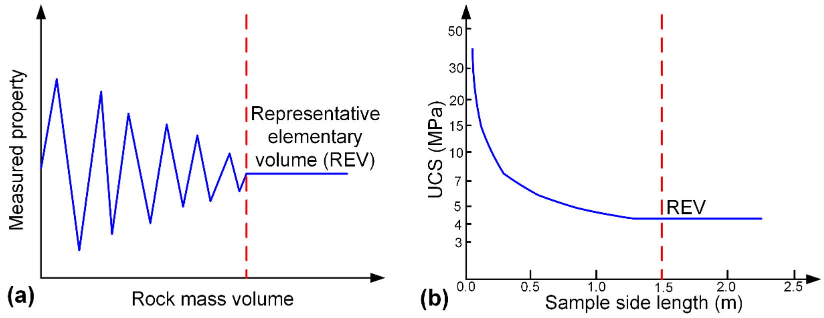

Figure 6. (**a**) Concept of the REV (after Bear, [49]). (**b**) The effect of sample size on the strength of coal (after Bieniawski, [50]).

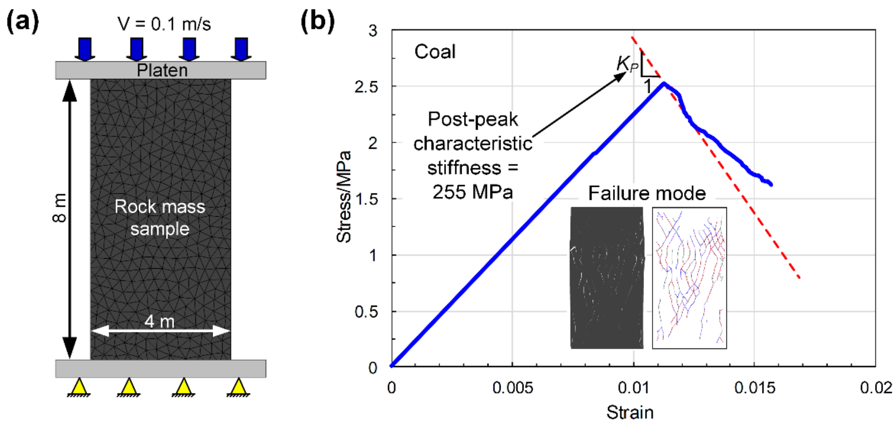

Figure 7. (**a**) UCS model. (**b**) Stress-strain curve of the coal mass sample under an ideal rigid loading condition.

3.1.3. Rock Mass Properties and Constitutive Model

The properties of rock masses (see Table 2) around the tunnel were obtained according to the laboratory tests of intact rock pieces (following ISRM recommended standards, [51]) and the generalized Hoek-Brown criterion [52] using the Geological Strength Index (*GSI*) system to evaluate rock mass qualities [53–55]. The UCS and deformation modulus of rock masses were estimated from the following equations [56,57]:

$$\sigma_{cm} = \sigma_{ci} \frac{(m_b + 4s - a(m_b - 8s))\left(\frac{m_b}{4+s}\right)^{as-1}}{2(1+a)(2+a)} \tag{3}$$

$$E_m = E_i\left(0.02 + \frac{1 - D/2}{1 + e^{((60+15D-GSI)/11)}}\right) \tag{4}$$

where D is a factor that depends upon the degree of disturbance to which the rock mass has been subjected by blast damage and stress relaxation. In this study, the value of D is assumed to be zero considering that the mechanical tunneling results in minimal disturbance to confined rock masses [56]. The calculated results of UCS and deformation modulus of rock masses are also summarized in Table 2.

The elastic constitutive model was chosen for blocks composed of finite-difference zones. The Coulomb slip model was used for contacts. The constitutive behavior of contacts is shown in Figure 8. A spring-rider simulates the behavior of contact, and the model deformation occurs when the contact stress is smaller than the contact strength, which is governed by the elastic modulus of blocks and contact stiffness; contact failure occurs when the stress exceeds its shear or tensile strength, and then blocks will slide or separate with each other [39].

Table 2. Physical and mechanical parameters of rock masses.

Lithology	Constant				Intact Rock				Rock Mass	
	m_i	m_b	s	a	ρ (kg/m^3)	σ_{ci} (MPa)	E_i (GPa)	v	σ_{cm} (MPa)	E_m (GPa)
Coal	17	1.729	0.0008	0.5	1300	9.3	1.86	0.30	2.50	0.23
Clay shale	9	1.327	0.0022	0.5	2500	29.0	5.62	0.31	7.93	1.26
Fine-grained sandstone	17	2.851	0.0039	0.5	2580	90.0	9.52	0.26	24.53	2.92
Sandy shale	12	1.877	0.0031	0.5	2530	26.0	5.23	0.25	7.11	1.42

Note: m_i is a material constant for intact rocks. m_b, s, and a are constants for rock masses. ρ is the bulk density of intact rocks. σ_{ci} is the UCS of intact rocks. E_i is Young's modulus of intact rocks. v is the Poisson's ratio of intact rocks. σ_{cm} is the UCS of rock masses and E_m stands for the deformation modulus of rock masses.

Table 3. Calibrated micro parameters of rock masses in the model.

Lithology	Block Properties			Contact Properties						
	ρ (kg/m^3)	K (GPa)	G (GPa)	k_n (GPa/m)	k_s (GPa/m)	c^j (MPa)	${c_r}^j$ (MPa)	φ^j (°)	${\sigma_t}^j$ (MPa)	${\sigma_{tr}}^j$ (MPa)
Coal	1300	0.16	0.09	18.7	7.5	0.99	0	33	0.25	0
Clay shale	2500	0.85	0.50	108.5	40.6	2.96	0	35	0.79	0
Fine-grained sandstone	2580	1.91	1.17	69.4	27.8	8.11	0	36	2.15	0
Sandy shale	2530	0.94	0.57	113.3	45.3	2.95	0	36	0.85	0

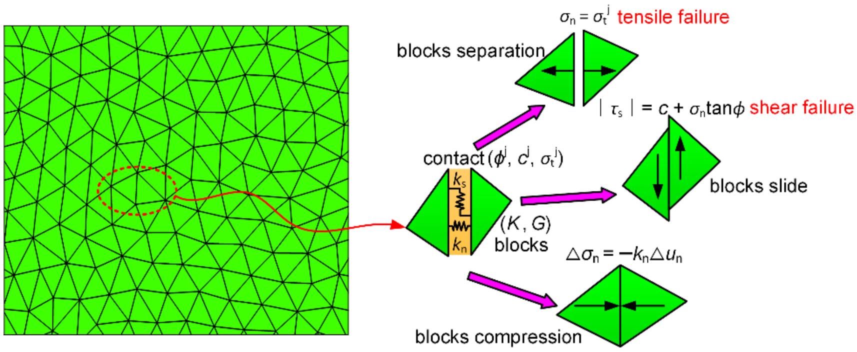

Figure 8. Constitutive behavior of contacts. (K and G are the bulk and shear moduli of blocks. c^j; Φ^j, and $\sigma_t{}^j$ are the cohesion force, internal friction angle, and tensile strength of contacts. $\Delta\sigma_n$ and Δu_n are the effective normal stress increment and normal displacement increment. σ_n and τ_s are the normal and shear stresses of contacts).

In the Trigon approach, the deformation and failure of rock masses depend on the properties of blocks and contacts [38,39]. Thus, the micro parameters of blocks and contacts were calibrated against the rock mass properties (Table 2). Next, simulated UCS tests were conducted to calibrate the micro parameters [38]. To eliminate the effect of block size on simulation accuracy, the calibration model had a large scale (4 m × 8 m) [40] and identical block size with the tunnel model. A displacement loading mode was used in the simulation by applying a constant velocity of 0.1 m/s to the surface of the top platen, and the bottom platen was fixed. The loading rate of 0.1–0.15 m/s is slow enough to avoid the dynamic responses of models because UDEC automatically selects very small time steps (e.g., 10^{-7} s) in static analysis [37,58]. The initial micro parameters were first assumed based on the macro parameters of rock masses. Then, the modeling of UCS tests was conducted iteratively with the adjustment of micro parameters until the simulated results were consistent with the targeted material properties. The simulated failure modes and stress-strain curves of rock mass samples are shown in Figure 9. The main failure modes of rock mass samples are tensile (axial splitting) and tensile-shear failure, consistent with typical rock mass failure modes under no or low confining pressures [59]. The calibrated micro parameters of rock masses are listed in Table 3. The targeted and simulated deformation modulus and UCS errors are less than 3% (Table 4), suggesting that the targeted values agree well with calibrated rock mass parameters. Thus, the calibrated micro parameters in Table 3 could be used for further numerical analysis to evaluate the performance of yielding rockbolts during self-initiated strainbursts.

Table 4. Comparison between the targeted and simulated rock mass parameters.

Lithology	**E_m (GPa)**			**UCS (MPa)**		
	Target	**Simulation**	**Error (%)**	**Target**	**Simulation**	**Error (%)**
Coal	0.23	0.226	0.09	2.50	2.51	0.48
Clay shale	1.26	1.234	−1.82	7.93	7.91	−0.29
Fine-grained sandstone	2.92	2.852	−2.48	24.53	24.52	−0.05
Sandy shale	1.42	1.39	−2.11	7.11	7.02	−1.27

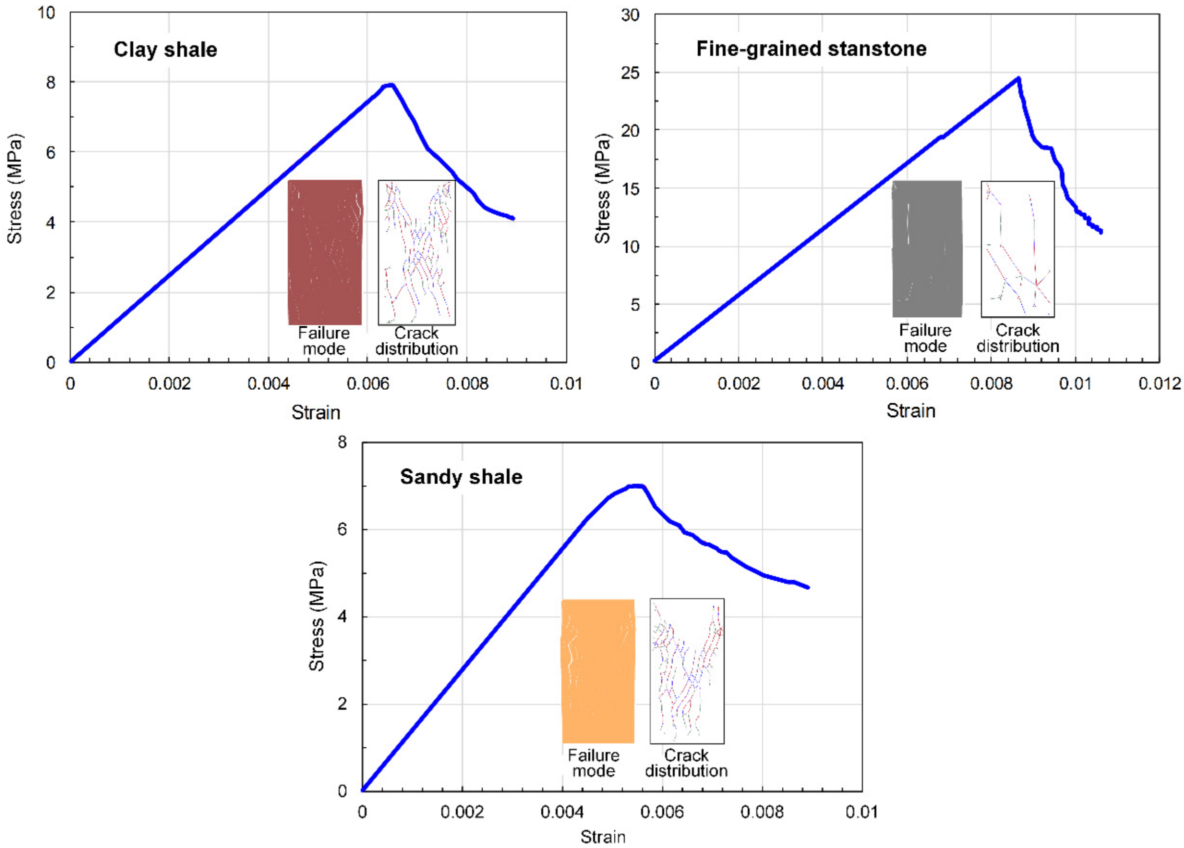

Figure 9. Simulated failure modes and stress-strain curves of rock mass samples.

3.2. Properties of Rockbolts

3.2.1. Introduction of the "Rockbolt" Element

In the past, the "cable" element in UDEC was more popular used than the "rockbolt" element to model a mechanically anchored or grouted cable or rockbolt, although both elements can simulate the shearing resistance along their length, which is provided by the shear bond between the grout and either the cable/rockbolt or the host rock [60]. This could be owing to more understandable input parameters and the more straightforward calibration process for using the "cable" element. Figure 10a shows the conceptual mechanical representation of the "rockbolt" element. It can be seen the "rockbolt" element is composed of several segments and nodal points located at segment ends. It has both shear and normal coupling springs, which are connectors that transfer forces and motion between the "rockbolt" element and the grid points associated with the block zone, while the "cable" element only has sliders (similar to shear coupling spring). Therefore, the "cable" element provides little resistance to bending, and thus it is more suitable for modeling cable bolts. In contrast, the "rockbolt" element can provide sufficient resistance for shearing and bending, appropriate for simulating rockbolts such as rebar bolts [61]. The other strength of the "rockbolt" element is that it can explicitly model the rockbolt breakage according to a user-defined tensile failure strain limit ε_{pl} [62]:

$$\varepsilon_{pl} = \sum \varepsilon_{pl}^{ax} + \sum \frac{d}{2} \frac{\theta_{pl}}{L} \tag{5}$$

where ε_{pl}^{ax} is the axial plastic strain of rockbolt segment elements; d is the rockbolt diameter; L is the rockbolt segment length; θ is the average angular rotation over the rockbolt. The tensile failure strain limit provides a more accurate and realistic approach to reproduce rockbolt performances. Thus, the "rockbolt" element was used in this study to simulate the mechanical behavior of both yielding and conventional rockbolts.

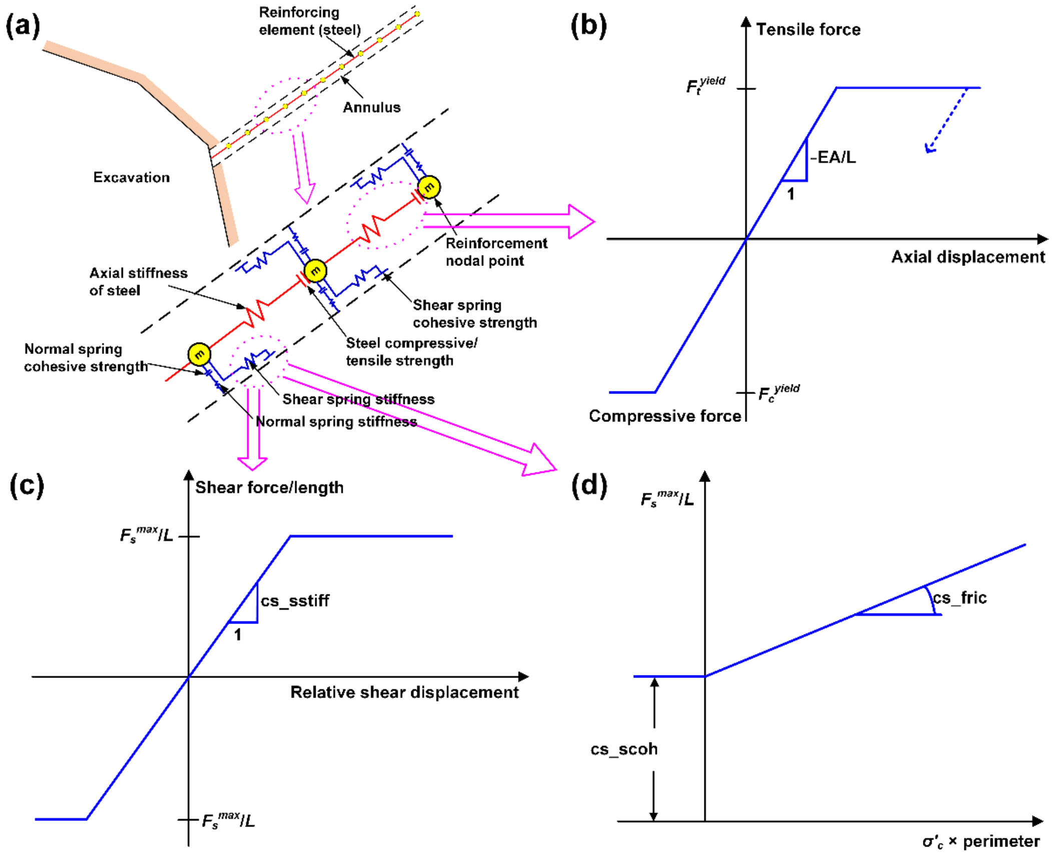

Figure 10. (**a**) Conceptual mechanical representation of the "rockbolt" element, which accounts for shear behavior of grout annulus and bending resistance of the reinforcement. (**b**) Mechanical behavior of the "rockbolt" element in the axial direction. (**c**) Shear force versus displacement of the shear coupling spring. (**d**) Shear criterion of the shear coupling spring ((**a**) is modified after Itasca [62]; (**b**–**d**) are from Itasca [62]).

The "rockbolt" element has a linearly elastic material behavior that it can yield in both tension and compression in the axial direction (Figure 10b). Therefore, the incremental axial force in a "rockbolt" element, ΔF_t, can be obtained by the calculation of the incremental axial displacement:

$$\Delta F_t = -\frac{EA}{L}\Delta u^t \tag{6}$$

where $\Delta u^t = \Delta u_i t_i = \Delta u_1 t_1 + \Delta u_2 t_2 = (u_1{}^{[b]} - u_1{}^{[a]})t_1 + (u_2{}^{[b]} - u_2{}^{[a]})t_2$; $u_1{}^{[b]}$, $u_1{}^{[a]}$, etc. are the displacements at the bolt nodes associated with each "rockbolt" element. Subscript 1 and 2 represent the x-direction and y-direction, respectively; the superscripts $[a]$, $[b]$ stand for bolt nodes. The direction cosines t_1, t_2 refer to the tangential (axial) direction of the "rockbolt" element.

The applied load is axial in an ideal pull-out test as simulated in this study. Thus, the parameters regarding resistance to bending (normal spring) are not discussed. The shear behavior of the "rockbolt" element were briefly introduced in this study. The shear behavior of the rockbolt/gridpoint interface is represented as a spring-slider system at the rockbolt nodal points. This behavior during relative displacement can be described numerically by the coupling spring shear stiffness (cs_{sstiff} in Figure 10c):

$$\frac{F_s}{L} = cs_{sstiff}\left(u_p - u_m\right) \tag{7}$$

where F_s represents the shear force that develops in the shear coupling spring (e.g., along with the interface between the rockbolt element and the gridpoint); cs_{sstiff} is the coupling spring shear stiffness (coupling-stiffness-shear); u_p is the axial displacement of the rockbolt; u_m is the axial displacement of the medium (soil or rock); and L is the contributing element length.

The maximum shear force that can be developed along the rockbolt/gridpoint interface is a function of the cohesive strength of the interface and the stress-dependent frictional resistance along with the interface (Figure 10d). The following equation can be used to determine the maximum shear force per length of the rockbolt:

$$\frac{F_s^{max}}{L} = cs_{scoh} + \sigma_c' \times tan\left(cs_{sfric}\right) \times perimeter \quad (8)$$

where cs_{scoh} is the cohesive strength of the shear coupling spring (coupling-cohesion-shear); σ_c' is the average effective confining stress perpendicular to the "rockbolt" element; cs_{sfric} is the friction angle of the shear coupling spring (coupling-friction-shear), and *perimeter* is the exposed perimeter of the element.

3.2.2. Calibration of Rockbolt Properties

The pull-out test is a well-recognized test, and it can represent the static load-displacement characteristics of rockbolts before rockbursting [63,64]. Besides, the performance of rockbolts during strainbursts has been initially confirmed by in situ observations and others' experimental test and simulation results in this research. Hence, only the simulated pull-out tests were conducted to calibrate the input parameters of the "rockbolt" element with the comparison of the laboratory test results from Charette and Plouffe [10], Stillborg [65], and Li [17]. The model's size is 2 m × 1 m, and the bolt length is 2 m. This model size is almost identical to Bahrani and Hadjigeorgiou [60]. The model has a Young's modulus of 7.5 GPa and a Poisson's ratio of 0.25 to represent an elastic rock mass because it has been confirmed that the elastic properties of the rock mass do not influence the load-displacement response of the "rockbolt" element [61] which can significantly save computation time. The rockbolt was divided into 40 segments and 41 nodes to ensure that at least one node falls into each block zone [60]. The upper boundary of the model was free, and a vertical upward velocity of 0.08 m/s was applied to the end node of the bolt to simulate a pull action [66]. The roller constraints were applied on the side boundaries and the bottom boundary was fixed. A function was developed using the FISH language (built-in programming package) in UDEC to monitor the axial force and displacement of the last segment of the rockbolt in y-direction.

The modeling of pull-out tests was conducted iteratively to adjust input parameters (e.g., tensile yield strength, tension failure strain, shear coupling spring stiffness, and shear coupling spring cohesion, [62]) until the simulated results were consistent with the targeted properties of rockbolts. Other input parameters (e.g., the diameter, length, density, and elastic modulus of rockbolts) are the same as those used in laboratory tests. The simulated load-displacement curves and axial force of rockbolts and the block displacement are shown in Figure 11. The calibrated input parameters of rockbolts are listed in Table 5. The applied load is axial in an ideal pull-test as simulated in this study. Thus, the parameters regarding resistance to bending are not employed. The errors between the targeted and simulated ultimate load, rupture displacement, and static energy-absorption capacity of rockbolts are less than 5% (Table 6), indicating that the targeted values agree well with calibrated input parameters. Thus, the calibrated parameters in Table 5 could be used to further the numerical analysis of the performance of yielding and conventional rockbolts [9]. However, it should be noted that the sliding or extraction of Roofex was not simulated explicitly in the pull-out test, and its energy-absorption mechanism was simplified to the deformation or stretch of bolt shanks. This equivalent approach could be regarded as a relatively good selection at this stage since the complexity of simulating bolt sliding was ignored, and the time cost was thus significantly reduced.

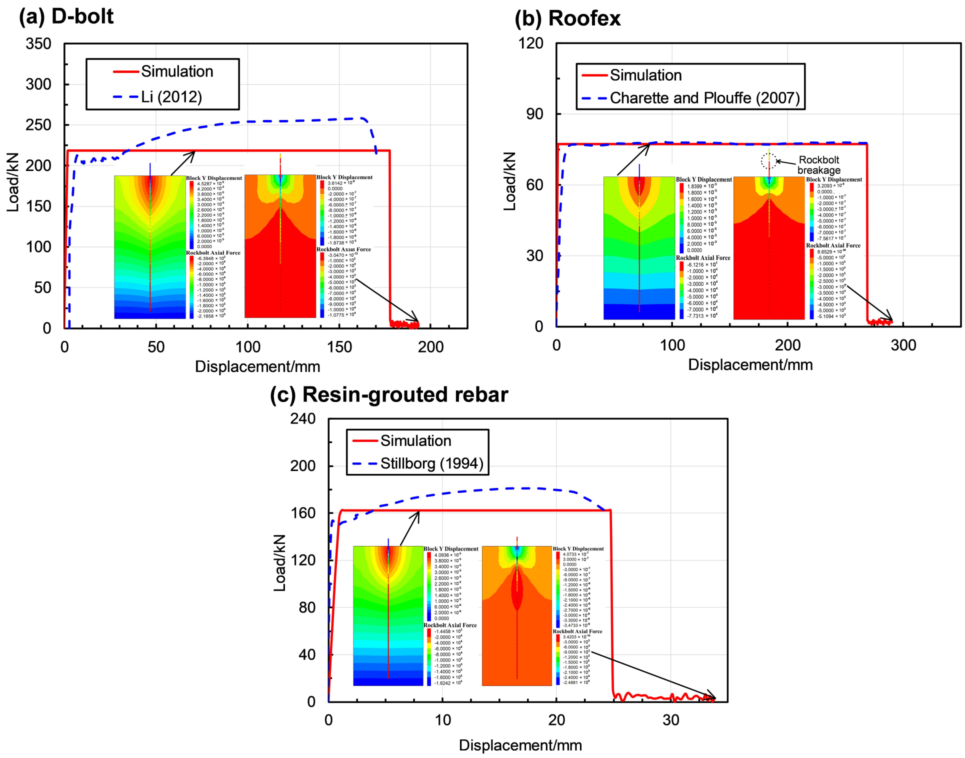

Figure 11. Simulated load-displacement curves and axial forces of rockbolts and deformation of rock masses. (Rockbolt axial force in N and block Y displacement in m.).

3.3. Simulation Procedures and Schemes

Modeling the effects of yielding rockbolts on controlling self-initiated strainbursts was performed with the following stages and schemes.

Stage I (static stage): The in situ stress field was applied to the model, and the geostatic equilibrium was achieved. Then, the tunnel was excavated by deleting the blocks. Adequate calculation steps were run to ensure gradual and slow release of surrounding rock stresses [38]. The installation of rockbolts was conducted immediately after the excavation of the tunnel.

Stage II (dynamic stage): The dynamic mode was activated. The local damping ratio was set 0.05. The viscous boundary [43] was used in the dynamic calculation to avoid propagating waves' reflection and allow the necessary energy radiation. The dynamic calculation time is set to 120 ms. The pattern layout of rockbolts in the tunnel is shown in Figure 4. The roof and two ribs of the tunnel were supported by 15 rockbolts in total, while the floor remained unsupported, as is a common practice. The roof and rib bolts have a length of 2.5 m and row spacing of 0.7 m. The spacing of rockbolts along the tunnel axis is one meter by setting the "spacing" parameter in UDEC. Besides, D-bolt, Roofex, and fully resin-grouted rebar were simulated in each scheme.

Table 5. Calibrated input parameters of rockbolts.

Rockbolt Type	Cross-Sectional Area (m^2)	Moment of Inertia (m^4)	Perimeter of Borehole (m)	Density (kg/m^3)	Elastic Modulus (GPa)	Tensile Yield Strength (kN)	Tension Failure Strain	Shear Coupling Spring Stiffness (GN/m/m)	Shear Coupling Spring Cohesion (kN/m)	Shear Coupling Spring Friction Angle (°)
Resin-grouted rebar	3.14×10^{-4}	7.85×10^{-9}	0.08	7500	200	517	0.33	0.31	400	45
D-bolt	3.80×10^{-4}	1.15×10^{-8}	0.10	7500	200	575	1.36	0.29	438	45
Roofex	1.23×10^{-4}	1.20×10^{-9}	0.08	7500	200	630	1.66	0.21	353	45

Table 6. Comparison between the targeted and simulated rockbolt properties.

Rockbolt Type	Ultimate Load (kN)			Rupture Displacement (mm)			Static Energy-Absorption Capacity (kJ)		
	Laboratory Test	Simulation	Error/(%)	Laboratory Test	Simulation	Error/(%)	Laboratory Test	Simulation	Error/(%)
Resin-grouted rebar	162	162	0.0	24.1	24.9	3.3	4.15	3.96	−4.6
D-bolt	212	219	3.3	170	178	4.7	40.23	38.65	−3.9
Roofex	77.6	77.3	−0.4	274	269	−1.8	20.94	20.71	−1.1

4. Analysis of Simulation Results

4.1. Displacement and Velocity Analysis

The simulated displacement patterns of the tunnel supported by different types of rockbolts are shown in Figure 12a. The large deformation only occurs in a local tunnel area that D-bolts support. In contrast, noticeable roof subsidence and sidewall shrinkage are observed when the tunnel is supported with Roofex and resin-grouted rebar. To further investigate the effects of different types of rockbolts on controlling strainbursts, four monitoring points were arranged at the roof, floor, and two sidewalls of the tunnel to record the tunnel deformation (Figure 4). The comparison of the tunnel deformation in three support schemes is shown in Figure 12b. It can be seen that the tunnel supported by D-bolts suffers minor deformation (1411 mm in total). However, the total deformations of the tunnel supported with Roofex and resin-grouted rebar are 2159 mm and 2946 mm, respectively, which are 1.53 and 2.09 times that of the tunnel supported by D-bolts.

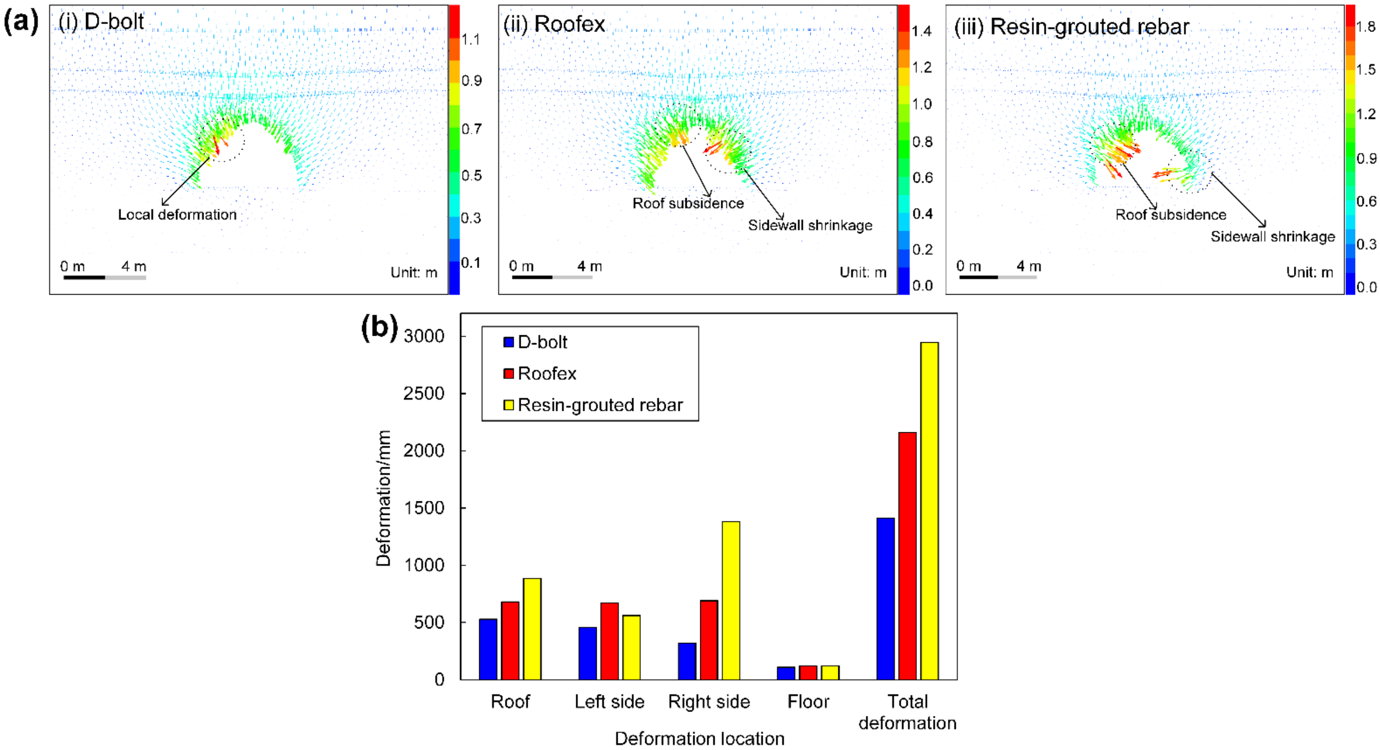

Figure 12. (**a**) Simulated displacement vectors of the surrounding rock masses along the tunnel supported by different types of rockbolts. (**b**). Comparison of the deformation of the tunnel supported by different types of rockbolts.

The most severe deformation is found when the resin-grouted rebar supports the tunnel. Although the resin-grouted rebar has relatively high strength (162 kN), its elongation rate is low and easy to break during dynamic shocks. As shown in Figure 13c, many resin-grouted rebar bolts are broken during the strainburst, and therefore they are unable to control rapid rock bulking or ejection effectively. Some in situ observations (see Figure 14) can confirm this phenomenon. Figure 14a shows that resin-grouted rebar bolts were broken in a rockburst while yielding rockbolts survive. Figure 14b,c also illustrate that many rebar bolts failed in rockbursts in deep tunnels. The match between simulation results and in situ observations verifies the reliability and rationality of the "rockbolt" element in modeling the performance of yielding rockbolts. Roofex also fails to restrain the large deformation because it possesses the lowest strength (77 kN) compared to D-bolt (219 kN) and resin-grouted rebar (162 kN). In summary, Roofex and resin-grouted rebar cannot effectively control the large deformation in self-initiated strainbursts.

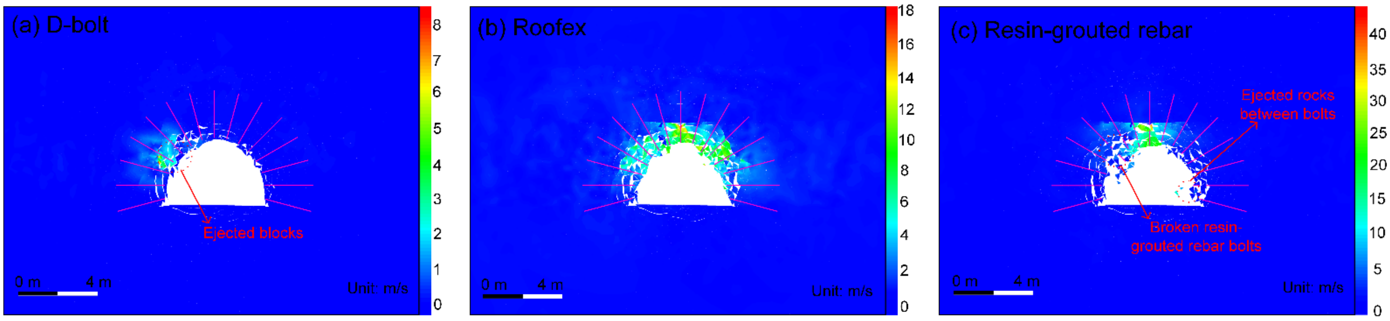

Figure 13. Simulated velocity distribution of the surrounding rock masses along the tunnel supported by different types of rockbolts. (**a**) D-bolt; (**b**) Roofex; (**c**) Resin-grouted rebar.

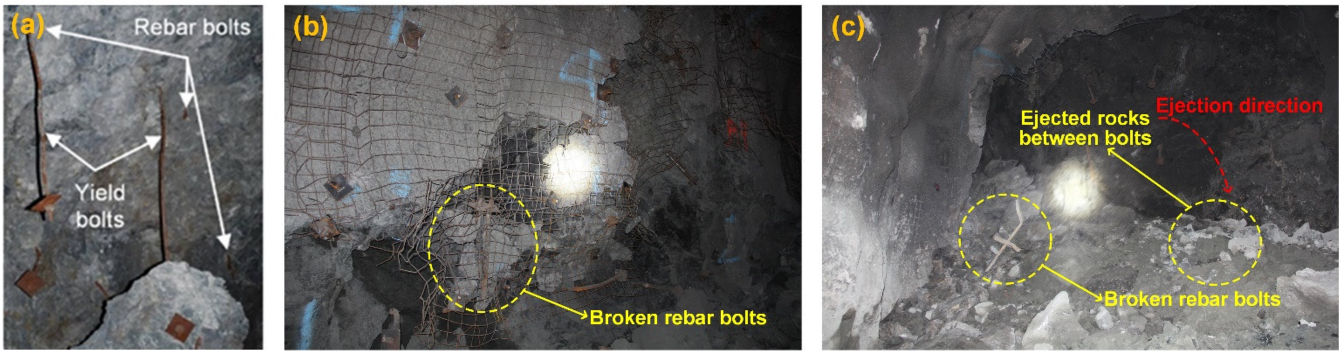

Figure 14. (**a**) Observed performance of fully resin-grouted rebar and yielding rockbolts in a rockburst [67]. (**b**,**c**) are in situ observations of broken rebar bolts after rockbursts in deep tunnels (photographs taken by authors).

The velocity distribution of tunnel surrounding rock masses in three support schemes is shown in Figure 13. It can be seen from Figure 13 that only a few rock blocks are ejected from a local zone when the D-bolt is adopted. For the tunnel supported by Roofex and resin-grouted rebar, much more rock blocks are ejected from the roof and sidewalls. To further study the effects of different rockbolts on mitigating rockburst damage, a function was developed using FISH language programming in UDEC to record the velocity and volume of all the detached rock blocks in the model. The detached rock blocks were detected when blocks or the clusters of blocks have no contact normal forces on their boundaries. The statistical analysis results are illustrated in Figure 15. As shown in Figure 15a, the average velocity of detached rock blocks in the tunnel supported by D-bolts is only 0.34 m/s, although a few blocks may have a relatively high velocity (e.g., 5–10 m/s). By comparison, the average velocities of detached rock blocks in the tunnel supported with Roofex and resin-grouted rebar are 3.22 and 3.97 m/s, respectively. Besides, the velocity distributions of rock blocks in these two scenarios are more extensive than those in the tunnel using D-bolts. Figure 15b shows that 99.8% of rock blocks in the tunnel supported by D-bolts possesses a velocity lower than 5 m/s, while the velocities of most rock blocks in the other two scenarios (95.1% for Roofex and 89.2% for resin-grouted rebar) are within the range of 0–10 m/s. In addition, many rock blocks focus on the volume range of 0.04–0.055 m^3. This is because the edge length of blocks near the tunnel was set to 0.3 m. These results suggest that the rock ejection is much more violent when the tunnel is supported by Roofex and resin-grouted rebar, which further confirms that these two types of rockbolts are unable to control strainbursts.

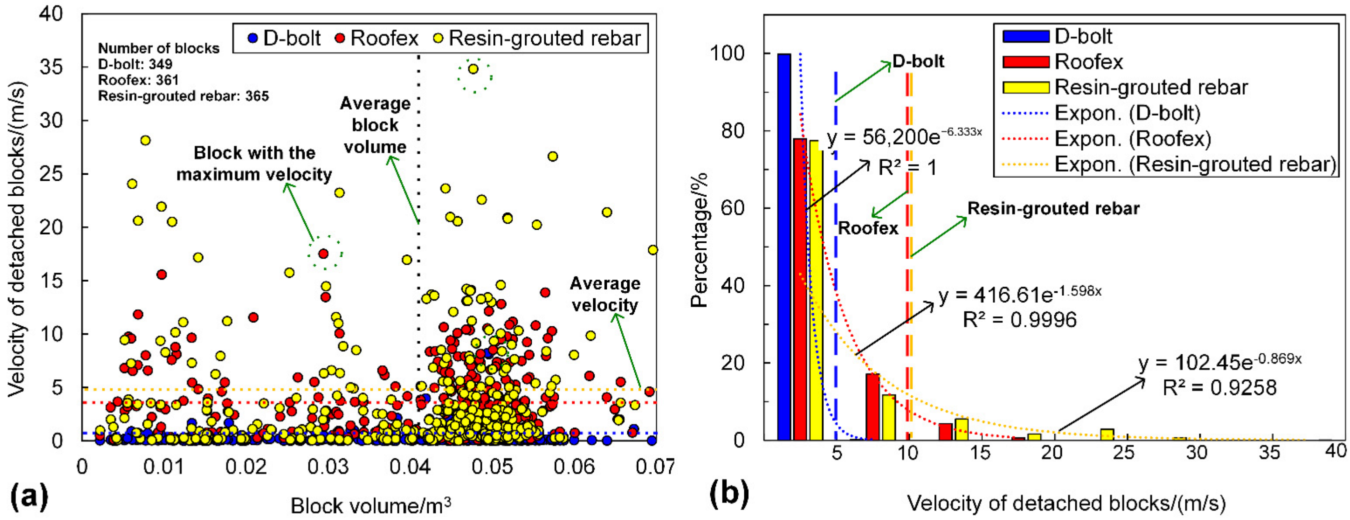

Figure 15. (**a**) is the velocity of all detached blocks versus block volume. (**b**) is the velocity distribution of all detached blocks. e is the Euler's number.

4.2. Rockburst Damage Analysis

In order to investigate the influences of different types of rockbolts on mitigating rockburst damage, the macroscopic failure pattern and damage degree of the tunnel induced by strainbursts were analyzed. In this study, the rockburst damage degree was evaluated by the volume of failed rocks [1]. A function was developed using FISH language programing in UDEC to sum the volume of detached rock blocks. It should be noted that the volume of detached rock blocks induced by static excavation was excluded in the calculation.

Figure 16 shows the macroscopic failure patterns of the tunnel supported by different types of rockbolts. As shown in Figure 16a, when D-bolts are adopted in the tunnel, the extent of the fractured zone is much smaller than that of the tunnel supported with Roofex and resin-grouted rebar. Only a few rock blocks are ejected between bolts, and the tunnel surrounding rock masses are overall stable. However, the surrounding rock masses are fractured for the tunnel using Roofex and resin-grouted rebar, and many ejected rock blocks are observed. As a result, the rockfall occurs, and the tunnel tends to be unstable.

The comparison of the volume of ejected rock blocks of the tunnel in three support schemes is shown in Figure 16b. The volume of ejected rock blocks is the least (1.07 m^3) when the tunnel uses D-bolt support. However, the volume of ejected rock blocks of the tunnel supported with Roofex and resin-grouted rebar is 1.54 m^3 and 1.79 m^3, respectively, which are 1.44 and 1.67 times that of the tunnel supported by D-bolts. The rockburst damage is the most serious when resin-grouted rebar supports the tunnel due to its low deformation capacity to restrain rapid rock bulking and ejection [1,7]. This finding further verifies that the conventional rockbolts (e.g., rebar bolts) are too stiff to control rockburst damage. Besides, the volume of ejected rock blocks of the tunnel supported with Roofex is moderate. This is because Roofex has the lowest strength, and its sliding mechanism can be easily activated. Thus, it is too "soft" or "smooth" to limit ejected rocks' movement compared to D-bolts.

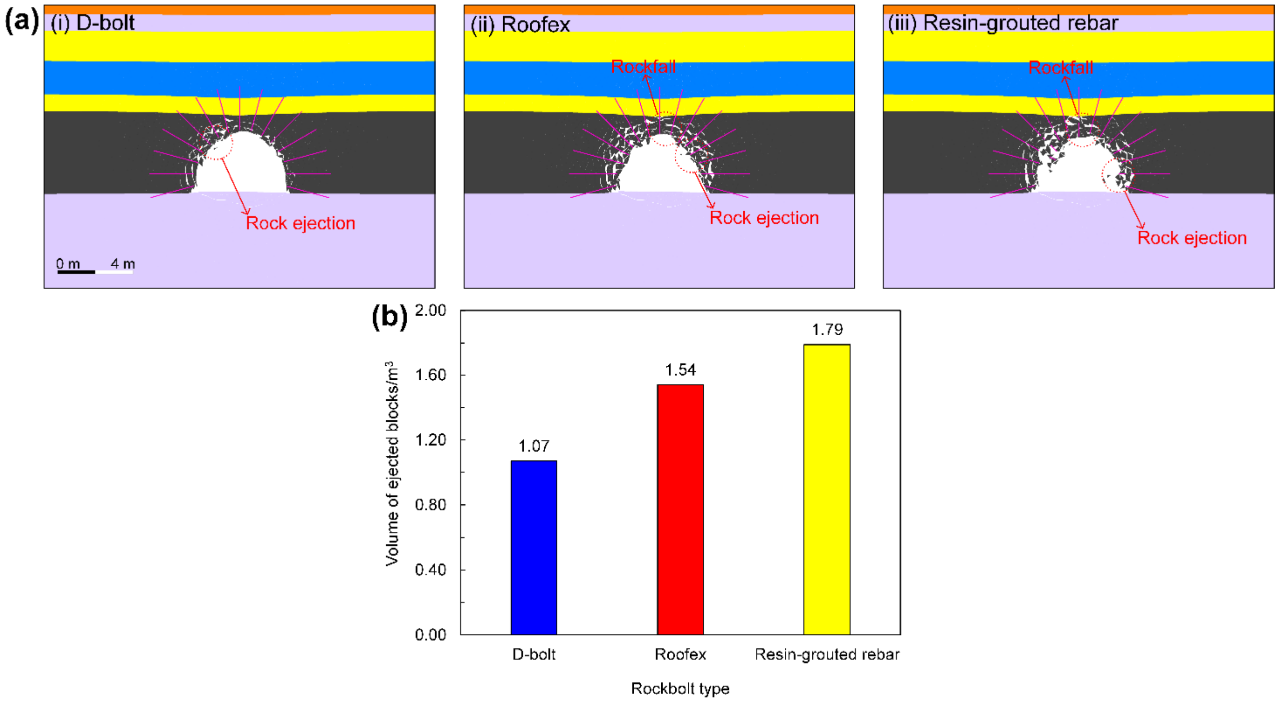

Figure 16. (**a**) Macroscopic failure patterns of the tunnel supported by different types of rockbolts. (**b**) is the volume of ejected rock blocks of the tunnel induced by rockbursts.

4.3. Energy Evolution Analysis

The severity of rockbursts is related to the magnitude of the kinetic energy of ejected rock materials [1,68]. The kinetic energy is one part of the total released energy that the whole supporting system (e.g., rockbolt, cable bolt, liner, and wire mesh) must absorb to reduce rockburst risks [69]. Therefore, the influences of rockbolt supporting on the distribution and change of kinetic energy were investigated in this study. The kinetic energy of ejected rock blocks was captured by the FISH language programing in UDEC using the following formula:

$$W_k = \sum \frac{1}{2} m v^2 \tag{9}$$

where m and v are the mass and velocity of ejected rock blocks at the current time step.

The distribution of the kinetic energy of ejected rock blocks in three support schemes is shown in Figure 17. It can be seen that the kinetic energy pattern is very similar to that of velocity (see Figure 13). As shown in Figure 17a, only a few rock blocks have relatively high kinetic energy when the D-bolt is adopted. On the other hand, more rock blocks possess higher kinetic energy for the tunnel supported by Roofex and resin-grouted rebar. The variation of kinetic energy with time influenced by different rockbolt types is illustrated in Figure 17b. When the tunnel is supported with D-bolts, kinetic energy evolution can be divided into two stages: the kinetic energy first increases to the peak value from 0 to 26 ms and then gradually declines to almost zero. For Roofex, the kinetic energy experiences fast growth, especially after 80 ms, and reaches the peak value at 103 ms. Then, the kinetic energy drops with time but is still high. When the tunnel is supported by resin-grouted rebar, the kinetic energy first increases rapidly to the peak value from 0 to 54 ms and then suffers a sudden drop. Then, it surges again at 100 ms.

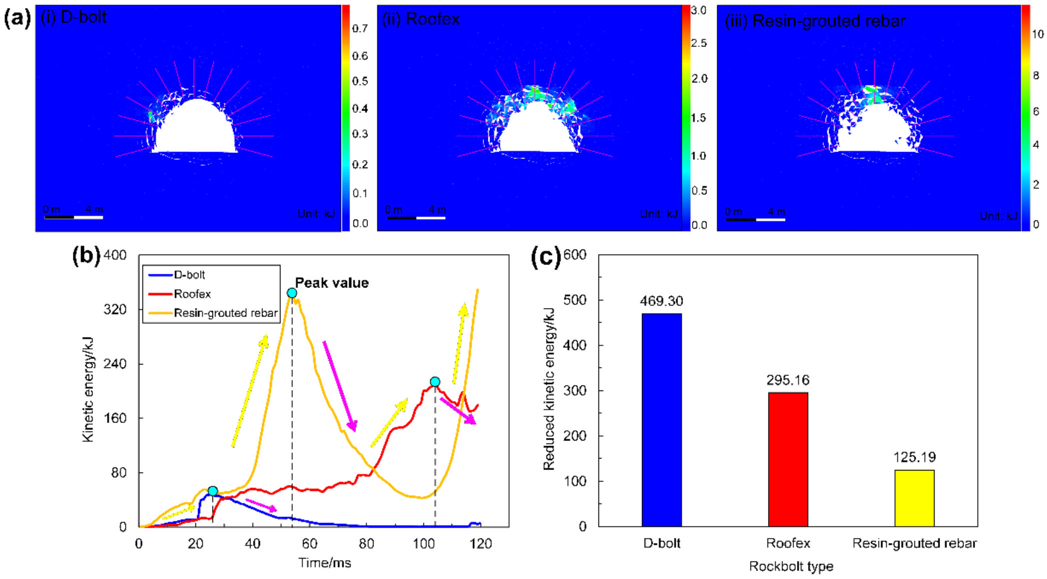

Figure 17. (**a**) Simulated kinetic energy distribution of ejected rock blocks in the tunnel supported by different types of rockbolts. (**b**) is the evolution of kinetic energy of ejected rock blocks. (**c**) is the comparison of reduced kinetic energy of ejected rock blocks.

Interestingly, kinetic energy grows again. This is because the ineffectiveness of resin-grouted rebar results in the "Domino-like" failure fashion during the strainburst. In summary, D-bolts absorb the kinetic energy of ejected rock blocks effectively, and the strainburst is controlled. However, Roofex and resin-grouted rebar fail to absorb the kinetic energy of ejected rock blocks effectively and cannot control the strainburst.

To further evaluate the dynamic energy-absorption capacity of three types of rockbolts, the tunnel without adopting any supports during the strainburst was simulated. Then, a new variable was defined as the reduced kinetic energy, which is the difference between the kinetic energy of ejected rock blocks in the tunnel without and using rockbolts. Figure 17c compares the reduced kinetic energy of ejected rock blocks in the tunnel supported by different rockbolts. The reduced kinetic energy is the highest (469.30 kJ) when the tunnel uses D-bolt support. In contrast, the reduced kinetic energy is the lowest (125.19 kJ) for the tunnel supported by resin-grouted rebar, while the performance of Roofex on reducing kinetic energy (295.16 kJ) is in between the D-bolt and resin-grouted rebar. These results are not surprising because they agree that D-bolt has both high strength and excellent deformation capacity, while Roofex has low strength and resin-grouted rebar has very limited deformation capacity.

4.4. Rockbolt Force Analysis

The simulated axial force distribution of rockbolts in three support schemes is shown in Figure 18. It can be seen that in all three cases, the tensile axial force tends to reach the peak value at a certain distance (around 1–1.5 m) from the bolt end (head) and then gradually decreases to a low value. The simulated axial force patterns of rockbolts agree with some published experimental test [70] and numerical simulation results [71,72]. The average peak values of axial forces for three rockbolt types are 214.87 kN, 76.99 kN, and 151.05 kN, respectively. Thus, both the D-bolt and resin-grouted rebar can bear the high load of rock masses, while the Roofex cannot provide sufficient resistance to control large rock deformation and rapid rock bulking during strainbursts.

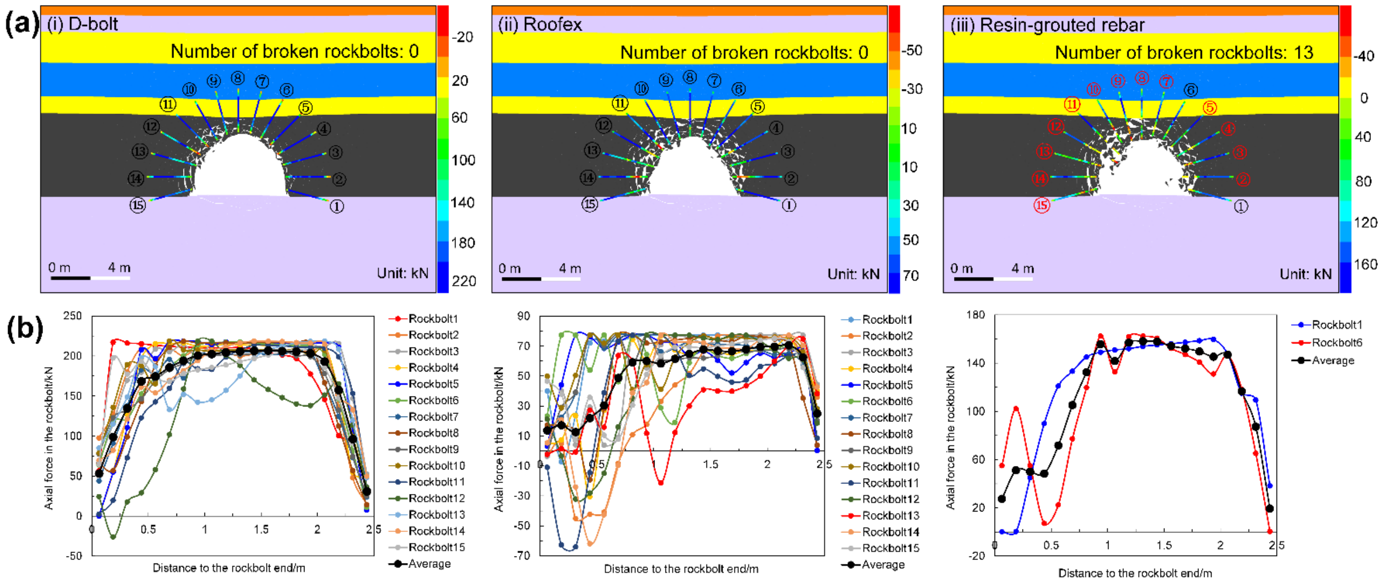

Figure 18. Simulated contours (**a**) and distribution of the axial force (**b**) in rockbolts for the tunnel supported by different rockbolts. The black and red numbers indicate intact and broken rockbolts, respectively. The positive value of axial forces represents a tensile load.

Additionally, it can be observed that 13 resin-grouted rebar bolts are broken, resulting in the unsuccessful control of the strainburst. Again, this is because the resin-grouted rebar has limited deformation capacity to accommodate rapid rock bulking and relieve rock ejection [1,7]. No broken rockbolts were found for the tunnel adopting D-bolt and Roofex supporting. In summary, the D-bolt and resin-grouted rebar can maintain a high axial force level during the strainburst to restrain rock ejection and rock bulking, but the resin-grouted rebar is prone to be broken due to a minimal elongate rate failing to mitigate rockburst damage effectively. Roofex's axial force is too low to control strainbursts, although it has an excellent deformation capacity over the other two rockbolt types.

5. Discussion

5.1. Influence of the Bolt Number

The effects of rockbolts on controlling self-initiated strainbursts not only depend on rockbolt types but also are affected by other factors, e.g., bolt number, bolt length, and row spacing. Therefore, it is interesting to explore the influences of these factors on the control and mitigation of strainburst damage, which can be used for optimizing the support design in burst-prone grounds. Since the D-bolt performs better on controlling strainbursts than Roofex and resin-grouted rebar based on previous analyses, it was decided to simulate the tunnel supported by D-bolts with different bolt numbers (9, 12, 15, and 18) as an example, while other influence factors (e.g., bolt length) can also be studied in the model.

The simulation results are shown in Figures 19 and 20. It can be seen from Figure 19a that many rock blocks with high velocities are ejected from the roof and sidewalls when 9 D-bolts support the tunnel. A moderate number of rock blocks are ejected from a local zone when 12 D-bolts are installed. However, only a few rock blocks are ejected for the tunnel supported with 15 D-bolts, and almost no ejected rock blocks are found when the bolt number is 18. The statistical analysis results of the velocity and volume of all the detached rock blocks in the model are illustrated in Figure 20. As shown in Figure 20a, the average velocity of rock blocks in the tunnel supported by 9 D-bolts is 4.54 m/s. By comparison, the average velocities of rock blocks in the tunnel supported with 12, 15, 18 D-bolts are 0.48, 0.34, and 0.04 m/s, respectively. These results suggest that the rock ejection is very violent when the tunnel is supported by 9 D-bolts, which fail to control the strainburst.

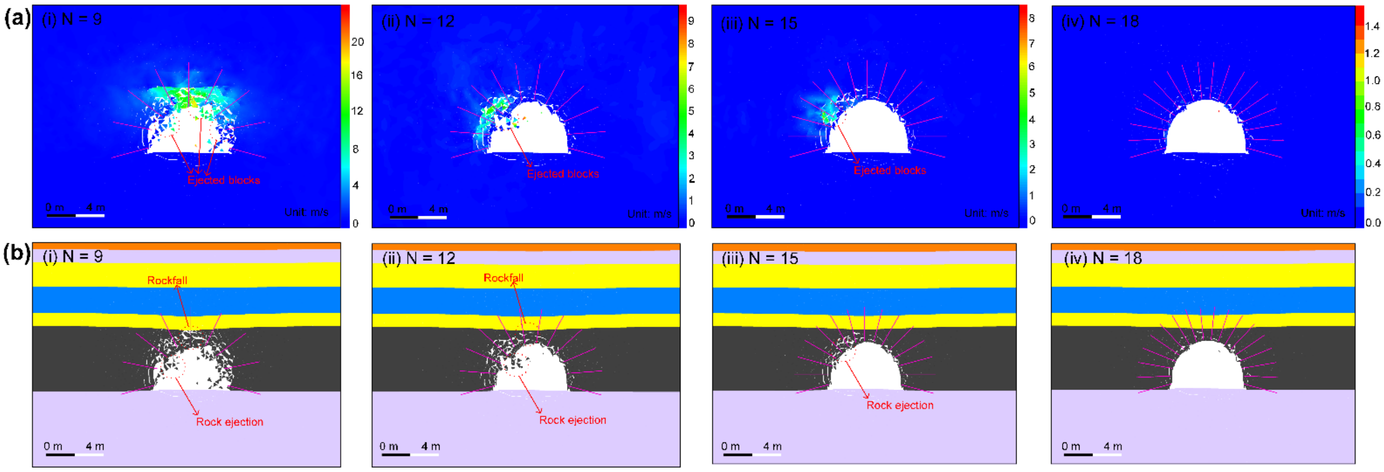

Figure 19. (**a**,**b**) are simulated velocity distribution and macroscopic failure patterns of the tunnel. N is the bolt number.

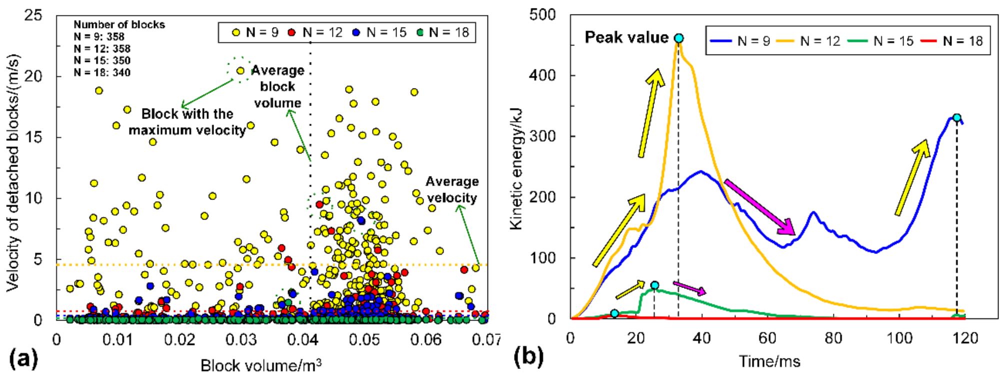

Figure 20. (**a**) is the velocity of all detached blocks versus block volume. (**b**) is the evolution of kinetic energy of ejected rock blocks in the tunnel. N is the bolt number.

Figure 19b shows the macroscopic failure patterns of the tunnel supported by different numbers of rockbolts. It can be seen that the extent of the fractured zone gradually decreases with the growth of bolt numbers. For the tunnel using 9 and 12 D-bolts, surrounding rock masses are very fractured, and rockfall and rock ejection are observed. The tunnel tends to be unstable. In contrast, only a few rock blocks are ejected when 15 D-bolts are installed. No obvious rockfall and rock ejection are observed, and the tunnel surrounding rock masses is very stable when the blot number is 18.

The variation of the kinetic energy of ejected rock blocks with time is illustrated in Figure 20b. When the tunnel is supported with 9 D-bolts, the kinetic energy first increases from 0 to 40 ms and then experiences several fluctuations. After that, the kinetic energy grows fast, especially after 100 ms, and reaches the peak value at 117 ms. In contrast, the kinetic energy evolution trends for the tunnel using 12, 15, and 18 bolts can all be divided into two stages: the kinetic energy first increases to the peak value and then gradually declines to lower values (almost zero when using 18 bolts). This is because more rockbolts are deformed to absorb the kinetic energy of ejected rock blocks, which the lower average velocity can confirm. However, the residual kinetic energy is still high (12.7 kJ) when adopting 12 D-bolts, indicating that this number is insufficient to control the strainburst. In summary, 9 and 12 D-bolts cannot control the strainburst, while 15 and 18 bolts can make the tunnel stable.

5.2. Influence of the Surface Retaining Element

The surface retaining element (e.g., fiber-reinforced shotcrete, wire mesh, and steel arch) is an indispensable component of the support system as it can prevent the unraveling of fractured rocks between rockbolts. Therefore, the effects of the combination of surface retaining elements and yielding rockbolts on controlling strainbursts should be investigated. In this research, the tunnel supported with D-bolts and a steel arch was simulated to demonstrate the benefits of surface retaining elements. The beam structural element modeled the steel arch in UDEC. The input parameters of the beam structural element are adopted from Małkowski et al. [53], as listed in Table 7.

Table 7. Input parameters of the beam structural element.

Input Parameter	Cross-Sectional Area (m^2)	Moment of Inertia (m^4)	Density (kg/m^3)	Poisson's Ratio	Elastic Modulus (GPa)	Tensile Yield Strength (kN)	Shear Coupling Spring Stiffness (GN/m/m)	Normal Coupling Spring Stiffness (GN/m/m)
Beam	4×10^{-3}	8.38×10^{-6}	7700	0.3	210	650	10^4	10^4

It should be noted that simulating both rockbolt and beam elements in the dynamic calculation mode in UDEC currently takes impracticable time (e.g., more than 1000 h) to approach the equilibrium state due to intrinsic difficulties in the program. Thus, the model's simulation results only running 20 ms were analyzed. Figure 21 shows the macroscopic failure patterns of the tunnel with and without a steel arch. It can be seen that the detachment and ejection of rock bocks between rockbolts are well restrained by the steel arch, although the surrounding rock masses are still fractured.

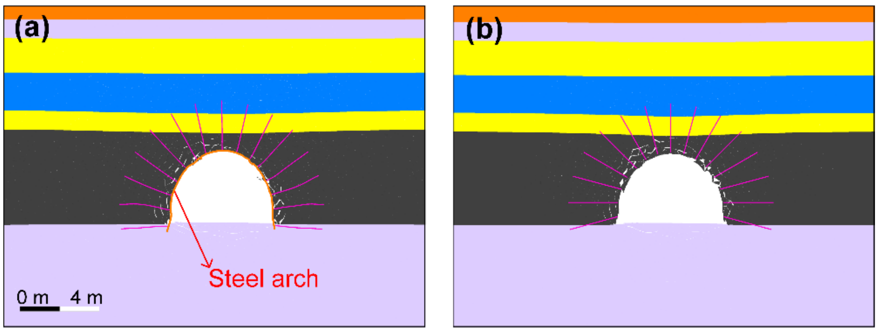

Figure 21. (**a**,**b**) are the macroscopic failure patterns of the tunnel with and without a steel arch. The dynamic calculation time is 20 ms.

5.3. Highlights and Limitations

The effects of yielding rockbolts on controlling self-initiated strainbursts were thoroughly numerically investigated using DEM. Instead of conventional drop tests, the performance of yielding rockbolts (e.g., the dynamic capacity of energy-absorption and control of rock damage) is evaluated during simulated strainbursts for the first time. The obtained results suggest that the D-bolt, as a type of high strength yielding rockbolt, can effectively control the large deformation, reduce kinetic energy, and mitigate rockburst damage, while Roofex (low strength yielding rockbolt) and resin-grouted rebar (stiff rockbolt) fail to control self-initiated strainbursts. This finding agrees well with many others' studies. For instance, Li et al. [21], Li [67], and Sharifzadeh et al. [22] suggested that the high strength yielding rockbolt should be used to control rockbursts, because this type of rockbolt can bear high loads and displace significantly, thereby absorbing a great amount of kinetic energy than other types of rockbolts.

This study highlights the usage of numerical modeling methods in assessing the performance of yielding rockbolts, which can be served as a promising tool to improve and optimize the design of rock supporting in burst-prone grounds following the presented modeling framework (including modeling sequence, parameter calibration method, model validation method, etc.). For example, the support scenarios with the combination of different bolt types (e.g., resin-grouted rebar and D-bolt), various bolt parameters (e.g., bolt number, bolt length, bolt strength, and row spacing), and surface retaining elements (e.g., fiber-reinforced shotcrete, wire mesh, and steel arch) can be modeled to select the optimal scheme that has best control effects and lowest cost.

The prerequisite for modeling self-initiated strainbursts is to determine whether the unstable failure will occur or not, which can be judged based on the local mine stiffness and the post-failure stiffness of rock masses. However, unlike the unstable failure of rock samples, it is hard to calculate the local mine stiffness when the focus is a strainburst that usually occurs in a tunnel or roadway. In this research, the authors first proposed a novel method to calculate the local mine stiffness of a tunnel: the ratio of the in situ stress at the designed excavation boundary to the convergence of tunnel walls. This method is straightforward, which can be easily fulfilled in 2D and 3D numerical modeling. The proposed method fills the gap about how to determine the local mine stiffness of a tunnel for modeling self-initiated strainbursts and provides a tool to predict the tendency of strainbursts using the stiffness theory during the design stage of mining and civil engineering projects.

The presented study and obtained results also point out some limitations for further research work:

1. The accuracy of simulation results can be improved if the dynamic mechanical properties of rock masses and joints and related constitutive relationships are known and used.
2. There is no energy dissipation when two contact faces are separated. Further studies (e.g., setting residual values of contacts or selecting more representative constitutive models) need to be conducted to consider the influences of fracture energy on simulation results.
3. The performance of yielding rockbolts during strainbursts has been initially confirmed by in situ observations and others' experimental test and simulation results. However, the simulation results will be more accurate and reliable if field monitoring data (e.g., dynamic strength and elongation rate) of yielding rockbolts during strainbursts are available to calibrate simulation parameters.
4. The sliding or extraction mechanism of Roofex should be simulated explicitly to better evaluate its performance during strainbursts. Setting reasonable parameters of the bolt-grout/rock interface will be a choice.
5. The performance of yielding rockbolts was mainly evaluated from the "macro" views of the dynamic energy-absorption capacity and the control of the deformation and damage of rock masses. Other "micro" behavior of rockbolts, e.g., the shear force and failure of bolt-grout/rock interfaces, can be studied in future research.

6. Conclusions

In this paper, a 2D DEM model of a deep tunnel in an underground coal mine is built to thoroughly evaluate the effects of yielding (D-bolt and Roofex) and the traditional rockbolt (fully resin-grouted rebar) on controlling self-initiated strainbursts. The occurrence of self-initiated strainbursts is judged based on the stiffness difference between the loading system and rock masses for the first time. The main conclusions are as follows:

(1) The total deformations of the tunnel supported with Roofex and resin-grouted rebar are 1.53 and 2.09 times that of D-bolts (1411 mm). The average velocities of detached rock blocks in the tunnel supported with Roofex and resin-grouted rebar are 3.22 and 3.97 m/s, respectively, which are much higher than that of D-bolts (0.34 m/s). 13 resin-grouted rebar bolts are broken during the strainburst, while D-bolts and Roofex

survive. This phenomenon agrees well with some in situ observations, verifying the reliability and rationality of the "rockbolt" element in modeling yielding rockbolts.

(2) The volume of ejected rock blocks can be obtained by the developed FISH function in the numerical model. The volume of ejected rock blocks in the tunnel supported by D-bolts is 1.07 m^3, which is the least compared with Roofex (1.54 m^3) and resin-grouted rebar (1.79 m^3).

(3) The dynamic energy-absorption capacity of rockbolts can be evaluated by a proposed variable, reduced kinetic energy. Compared with Roofex (295.16 kJ) and resin-grouted rebar (125.19 kJ), the D-bolt can reduce the most kinetic energy (469.30 kJ).

(4) The simulated axial force patterns of rockbolts agree with some published experimental test and numerical simulation results. The average peak values of axial forces for D-bolt, Roofex, and resin-grouted rebar are 214.87 kN, 76.99 kN, and 151.05 kN, respectively.

(5) The bolt number significantly influences the control effects of yielding rockbolts on strainbursts. For example, 9 and 12 D-bolts cannot control the strainburst, while 15 and 18 D-bolts can make the tunnel stable. In addition, the detachment and ejection of rocks between rockbolts can be well restrained using surface retain elements, e.g., steel arch.

In summary, D-bolt can effectively control the large deformation, reduce kinetic energy, and mitigate rockburst damage, while Roofex and resin-grouted rebar fail to control self-initiated strainbursts. This study highlights the usage of numerical modeling methods in assessing the performance of yielding rockbolts, which can be served as a promising tool to improve and optimize the design of rock supporting in burst-prone grounds.

Author Contributions: Conceptualization, J.W. and D.B.A.; methodology, J.W.; software, J.W.; validation, J.W., H.X. and C.W.; writing—original draft preparation, J.W.; writing—review and editing, H.X., C.W., K.S. and D.B.A.; supervision, D.B.A. All authors have read and agreed to the published version of the manuscript.

Funding: This research was funded by China Scholarship Council (funding number: 201808370185).

Data Availability Statement: All data is presented within the paper.

Acknowledgments: The first author thanks for Itasca Consulting Group, Inc. for a software loan within the Itasca Educational Partnership (IEP).

Conflicts of Interest: The authors declare no conflict of interest.

References

1. Cai, M. Principles of rock support in burst-prone ground. *Tunn. Undergr. Space Technol.* **2013**, *36*, 46–56. [CrossRef]
2. Zhang, C.; Feng, X.T.; Zhou, H.; Qiu, S.; Wu, W. Case Histories of Four Extremely Intense Rockbursts in Deep Tunnels. *Rock Mech. Rock Eng.* **2012**, *45*, 275–288. [CrossRef]
3. Wang, J.; Apel, D.B.; Dyczko, A.; Walentek, A.; Prusek, S.; Xu, H.; Wei, C. Investigation of the Rockburst Mechanism of Driving Roadways in Close-Distance Coal Seam Mining Using Numerical Modeling Method. *Min. Metall. Explor.* **2021**, *38*, 1899–1921. [CrossRef]
4. Kaiser, P.K.; McCreath, D.; Tannant, D. *Canadian Rockburst Support Handbook*; Geomechanics Research Center: Sudbury, ON, Canada, 1996.
5. Kaiser, P.K.; Cai, M. Design of rock support system under rockburst condition. *J. Rock Mech. Geotech. Eng.* **2012**, *4*, 215–227. [CrossRef]
6. Mutke, G.; Dubiński, J.; Lurka, A. New Criteria to Assess Seismic and Rock Burst Hazard in Coal Mines/Nowe Kryteria Dla Oceny Zagrożenia Sejsmicznego I Tąpaniami W Kopalniach Węgla Kamiennego. *Arch. Min. Sci.* **2015**, *60*, 743–760. [CrossRef]
7. Diederichs, M.S. Early assessment of dynamic rupture hazard for rockburst risk management in deep tunnel projects. *J. S. Afr. Inst. Min. Metall.* **2018**, *118*, 193–204. [CrossRef]
8. Ortlepp, W. The design of support for the containment of rockburst damage in tunnels: An engineering approach. In *International Symposium on Rock Support*; Balkema: Rotterdam, The Netherlands, 1992.
9. Atlas Copco Construction Mining Technique. Roofex Rock Bolt. Available online: https://www.forconstructionpros.com/equipment/underground/vertical-drilling-equipment/product/10080325/atlas-copco-construction-mining-technique-usa-llc-roofex-rock-bolt (accessed on 22 May 2021).

10. Charette, F.; Plouffe, M. Roofex®–Results of laboratory testing of a new concept of yieldable tendon. In Proceedings of the Fourth International Seminar on Deep and High Stress Mining, Perth, Australia, 7–9 November 2007.
11. Varden, R.; Lachenicht, R.; Player, J.; Thompson, A.; Villaescusa, E. Development and implementation of the garford dynamic bolt at the kanowna belle mine. In Proceedings of the 10th Underground Operators Conference, Launceston, Australia, 14–16 April 2008.
12. Li, C.C.; Doucet, C. Performance of D-Bolts Under Dynamic Loading. *Rock Mech. Rock Eng.* **2011**, *45*, 193–204. [CrossRef]
13. Normet. Normet D-Bolt®—Dynamic Rock Bolt. Available online: https://www.normet.com/product/d-bolt/ (accessed on 22 May 2021).
14. Wu, R.; Oldsen, J.; Campoli, A. Application of yield-lok bolt for bursting and convergence grounds in mines. In Proceedings of the 30th International Conference on Ground Control in Mining, Morgantown, WV, USA, 26 July 2011.
15. He, M.; Xia, H.; Jia, X.; Gong, W.; Zhao, F.; Liang, K. Studies on classification, criteria and control of rockbursts. *J. Rock Mech. Geotech. Eng.* **2012**, *4*, 97–114. [CrossRef]
16. Kang, H.; Lin, J.; Wu, Y. High pretensioned stress and intensive cable bolting technology set in full section and application in entry affected by dynamic pressure. *J. China Coal Soc.* **2009**, *34*, 1153–1159.
17. Li, C.C. Performance of D-bolts Under Static Loading. *Rock Mech. Rock Eng.* **2011**, *45*, 183–192. [CrossRef]
18. Wu, Y.; Gao, F.; Chen, J.; He, J. Experimental Study on the Performance of Rock Bolts in Coal Burst-Prone Mines. *Rock Mech. Rock Eng.* **2019**, *52*, 3959–3970. [CrossRef]
19. Zhang, P.; Nordlund, E. Numerical investigation of dynamic response of a rockbolt under drop testing and simulated seismic loading conditions. In Proceedings of the Ninth International Symposium on Ground Support in Mining and Underground Construction, Perth, Australia, 23–25 October 2019.
20. Cai, M.; Champaigne, D.; Kaiser, P.K. Development of a fully debonded cone bolt for rockburst support. In Proceedings of the Fifth International Seminar on Deep and High Stress Mining, Santiago, MN, USA, 6–8 October 2010.
21. Li, C.C.; Stjern, G.; Myrvang, A. A review on the performance of conventional and energy-absorbing rockbolts. *J. Rock Mech. Geotech. Eng.* **2014**, *6*, 315–327. [CrossRef]
22. Sharifzadeh, M.; Lou, J.; Crompton, B. Dynamic performance of energy-absorbing rockbolts based on laboratory test results. Part I: Evolution, deformation mechanisms, dynamic performance and classification. *Tunn. Undergr. Space Technol.* **2020**, *105*, 103510. [CrossRef]
23. Bosman, K.; Cawood, M.; Berghorst, A. Relationship between energy per impulse and dynamic capacity of a rockbolt. In Proceedings of the Rock Dynamics–Experiments, Theories and Applications, Trondholm, Norway, 13 July 2018.
24. Wang, J.; Apel, D.B.; Pu, Y.; Hall, R.; Wei, C.; Sepehri, M. Numerical modeling for rockbursts: A state-of-the-art review. *J. Rock Mech. Geotech. Eng.* **2021**, *13*, 457–478. [CrossRef]
25. Ji, S.; Karlovšek, J. Calibration and uniqueness analysis of microparameters for DEM cohesive granular material. *Int. J. Min. Sci. Technol.* **2022**, *32*, 121–136. [CrossRef]
26. Ji, S.; Karlovšek, J. Optimized differential evolution algorithm for solving DEM material calibration problem. *Eng. Comput.* **2022**. [CrossRef]
27. Wang, J.; Apel, D.B.; Dyczko, A.; Walentek, A.; Prusek, S.; Xu, H.; Wei, C. Analysis of the damage mechanism of strainbursts by a global-local modelling approach. *J. Rock Mech. Geotech. Eng.* **2022**. [CrossRef]
28. Manouchehrian, A. Numerical Modeling of Unstable Rock Failure. Ph.D. Thesis, Laurentian University, Sudbury, ON, Canada, 2016.
29. Nie, W.; Zhao, Z.Y.; Ning, Y.J.; Guo, W. Numerical studies on rockbolts mechanism using 2D discontinuous deformation analysis. *Tunn. Undergr. Space Technol.* **2014**, *41*, 223–233. [CrossRef]
30. Marambio, E.; Vallejos, J.; Burgos, L.; Gonzalez, C.; Castro, L.; Saure, J.; Urzua, J. Numerical modelling of dynamic testing for rock reinforcement used in underground excavations. In Proceedings of the Fourth International Symposium on Block and Sublevel Caving, Australian Centre for Geomechanics, Vancouver, BC, Canada, 15–17 October 2018.
31. Yokota, Y.; Zhao, Z.; Nie, W.; Date, K.; Iwano, K.; Koizumi, Y.; Okada, Y. Development of a new deformation-controlled rockbolt: Numerical modelling and laboratory verification. In Proceedings of the Ninth International Symposium on Ground Support in Mining and Underground Construction, Australian Centre for Geomechanics, Sudbury, ON, Canada, 23–25 October 2019.
32. Zhao, T.; Xing, M.; Guo, W.; Wang, C.; Wang, B. Anchoring effect and energy-absorbing support mechanism of large deformation bolt. *J. Cent. South Univ.* **2021**, *28*, 572–581. [CrossRef]
33. Su, G.; Jiang, J.; Zhai, S.; Zhang, G. Influence of Tunnel Axis Stress on Strainburst: An Experimental Study. *Rock Mech. Rock Eng.* **2017**, *50*, 1551–1567. [CrossRef]
34. Su, G.; Zhai, S.; Jiang, J.; Zhang, G.; Yan, L. Influence of Radial Stress Gradient on Strainbursts: An Experimental Study. *Rock Mech. Rock Eng.* **2017**, *50*, 2659–2676. [CrossRef]
35. Hu, L.; Ma, K.; Liang, X.; Tang, C.; Wang, Z.; Yan, L. Experimental and numerical study on rockburst triggered by tangential weak cyclic dynamic disturbance under true triaxial conditions. *Tunn. Undergr. Space Technol.* **2018**, *81*, 602–618. [CrossRef]
36. Hu, L.; Liang, X.; Liang, Z.; Li, Y.; Zhang, Z.; Tang, C.A. Influence of radial stress on strainbursts under true triaxial conditions: Insights from a distinct element modelling. *Int. J. Rock Mech. Min. Sci.* **2021**, *138*, 104577. [CrossRef]
37. Hu, L.; Su, G.; Liang, X.; Li, Y.; Yan, L. A distinct element based two-stage-structural model for investigation of the development process and failure mechanism of strainburst. *Comput. Geotech.* **2020**, *118*, 103333. [CrossRef]
38. Gao, F.; Stead, D.; Kang, H. Numerical Simulation of Squeezing Failure in a Coal Mine Roadway due to Mining-Induced Stresses. *Rock Mech. Rock Eng.* **2015**, *48*, 1635–1645. [CrossRef]

39. Chen, M.; Yang, S.Q.; Zhang, Y.C.; Zang, C.W. Analysis of the failure mechanism and support technology for the Dongtan deep coal roadway. *Geomech. Eng.* **2016**, *11*, 401–420. [CrossRef]
40. Yang, S.Q.; Chen, M.; Jing, H.W.; Chen, K.F.; Meng, B. A case study on large deformation failure mechanism of deep soft rock roadway in Xin'An coal mine, China. *Eng. Geol.* **2017**, *217*, 89–101. [CrossRef]
41. Stavrou, A.; Vazaios, I.; Murphy, W.; Vlachopoulos, N. Refined approaches for estimating the strength of rock blocks. *Geotech. Geol. Eng.* **2019**, *37*, 5409–5439. [CrossRef]
42. Xu, Y.H.; Cai, M. Influence of Loading System Stiffness on Post-peak Stress–Strain Curve of Stable Rock Failures. *Rock Mech. Rock Eng.* **2017**, *50*, 2255–2275. [CrossRef]
43. Lysmer, J.; Kuhlemeyer, R.L. Finite dynamic model for infinite media. *J. Eng. Mech. Div.* **1969**, *95*, 859–877. [CrossRef]
44. Itasca. *Introductory Training Course UDEC7/3DEC7*; Itasca Consulting Group, Inc.: Minneapolis, MN, USA, 2021.
45. Dai, L.; Pan, Y.; Li, Z.; Wang, A.; Xiao, Y.; Liu, F.; Shi, T.; Zheng, W. Quantitative mechanism of roadway rockbursts in deep extra-thick coal seams: Theory and case histories. *Tunn. Undergr. Space Technol.* **2021**, *111*, 103861. [CrossRef]
46. Cook, N.G. The failure of rock. *Int. J. Rock Mech. Min. Sci. Geomech. Abstr.* **1965**, *2*, 389–403. [CrossRef]
47. Jaiswal, A.; Shrivastva, B.K. Stability analysis of the proposed hybrid method of partial extraction for underground coal mining. *Int. J. Rock Mech. Min. Sci.* **2012**, *52*, 103–111. [CrossRef]
48. Farahmand, K.; Vazaios, I.; Diederichs, M.S.; Vlachopoulos, N. Investigating the scale-dependency of the geometrical and mechanical properties of a moderately jointed rock using a synthetic rock mass (SRM) approach. *Comput. Geotech.* **2018**, *95*, 162–179. [CrossRef]
49. Bear, J. *Dynamics of Fluids in Porous Media*; Dover Publication: New York, NY, USA, 1972.
50. Bieniawski, Z. The effect of specimen size on compressive strength of coal. *Int. J. Rock Mech. Min. Sci. Geomech. Abstr.* **1968**, *5*, 325–335. [CrossRef]
51. Fairhurst, C.; Hudson, J.A. Draft ISRM suggested method for the complete stress-strain curve for intact rock in uniaxial compression. *Int. J. Rock Mech. Min. Sci.* **1999**, *36*, 279–289.
52. Marinos, P.; Hoek, E. GSI: A geologically friendly tool for rock mass strength estimation. In Proceedings of the ISRM International Symposium, Melbourne, Australia, 19 November 2000.
53. Małkowski, P.; Ostrowski, Ł.; Bachanek, P. Modelling the small throw fault effect on the stability of a mining roadway and its verification by in situ investigation. *Energies* **2017**, *10*, 2082.
54. Małkowski, P.; Ostrowski, Ł. Convergence monitoring as a basis for numerical analysis of changes of rock-mass quality and Hoek-Brown failure criterion parameters due to longwall excavation. *Arch. Min. Sci.* **2019**, *64*, 93–118.
55. Szott, W.; Słota-Valim, M.; Gołąbek, A.; Sowiżdżał, K.; Łętkowski, P. Numerical studies of improved methane drainage technologies by stimulating coal seams in multi-seam mining layouts. *Int. J. Rock Mech. Min. Sci.* **2018**, *108*, 157–168. [CrossRef]
56. Hoek, E.; Carranza-Torres, C.; Corkum, B. Hoek-Brown failure criterion-2002 edition. In Proceedings of the NARMS-Tac, Toronto, ON, Canada, 10 July 2002.
57. Hoek, E.; Diederichs, M. Empirical estimation of rock mass modulus. *Int. J. Rock Mech. Min. Sci.* **2006**, *43*, 203–215. [CrossRef]
58. Gao, F.; Kaiser, P.K.; Stead, D.; Eberhardt, E.; Elmo, D. Strainburst phenomena and numerical simulation of self-initiated brittle rock failure. *Int. J. Rock Mech. Min. Sci.* **2019**, *116*, 52–63. [CrossRef]
59. Diederichs, M.S. The 2003 Canadian Geotechnical Colloquium: Mechanistic interpretation and practical application of damage and spalling prediction criteria for deep tunnelling. *Can. Geotech. J.* **2007**, *44*, 1082–1116. [CrossRef]
60. Bahrani, N.; Hadjigeorgiou, J. Explicit reinforcement models for fully-grouted rebar rock bolts. *J. Rock Mech. Geotech. Eng.* **2017**, *9*, 267–280. [CrossRef]
61. Tomasone, P.; Bahrani, N.; Hadjigeorgiou, J. Practical considerations in the modelling of resin-grouted rockbolts. *J. S. Afr. Inst. Min. Metall.* **2020**, *120*, 385–392. [CrossRef] [PubMed]
62. Itasca. *UDEC, Version 7.0 Manual*; Itasca Consulting Group, Inc.: Minneapolis, MN, USA, 2020.
63. Skrzypkowski, K.; Korzeniowski, W.; Zagórski, K.; Zagórska, A. Modified Rock Bolt Support for Mining Method with Controlled Roof Bending. *Energies* **2020**, *13*, 1868. [CrossRef]
64. Skrzypkowski, K. An Experimental Investigation into the Stress-Strain Characteristic under Static and Quasi-Static Loading for Partially Embedded Rock Bolts. *Energies* **2021**, *14*, 1483. [CrossRef]
65. Stillborg, B. *Professional Users Handbook for RockBolting*; Trans Tech Publications: Clausthal, Germany, 1994.
66. Zhu, D.; Wu, Y.; Liu, Z.; Dong, X.; Yu, J. Failure mechanism and safety control strategy for laminated roof of wide-span roadway. *Eng. Fail. Anal.* **2020**, *111*, 104489. [CrossRef]
67. Li, C.C. Principles and methods of rock support for rockburst control. *J. Rock Mech. Geotech. Eng.* **2020**, *13*, 46–59. [CrossRef]
68. Gao, F.; Kaiser, P.K.; Stead, D.; Eberhardt, E.; Elmo, D. Numerical simulation of strainbursts using a novel initiation method. *Comput. Geotech.* **2019**, *106*, 117–127. [CrossRef]
69. Raffaldi, M.; Chambers, D.; Johnson, J. Numerical study of the relationship between seismic wave parameters and remotely triggered rockburst damage in hard rock tunnels. In Proceedings of the Eighth International Conference on Deep and High Stress Mining, Australian Centre for Geomechanics, Perth, Australia, 28–30 March 2017.
70. Hyett, A.; Moosavi, M.; Bawden, W. Load distribution along fully grouted bolts, with emphasis on cable bolt reinforcement. *Int. J. Numer. Anal. Methods Geomech.* **1996**, *20*, 517–544. [CrossRef]

71. Lisjak, A.; Young-Schultz, T.; Li, B.; He, L.; Tatone, B.S.A.; Mahabadi, O.K. A novel rockbolt formulation for a GPU-accelerated, finite-discrete element method code and its application to underground excavations. *Int. J. Rock Mech. Min. Sci.* **2020**, *134*, 104410. [CrossRef]
72. Ma, S.; Nemcik, J.; Aziz, N. Simulation of fully grouted rockbolts in underground roadways using FLAC2D. *Can. Geotech. J.* **2014**, *51*, 911–920. [CrossRef]